Chapter 11

Processing of Ice Cloud In Situ Data Collected by Bulk Water, Scattering, and Imaging Probes: Fundamentals, Uncertainties, and Efforts toward Consistency

GREG M. MCFARQUHAR,[a,b,m] DARREL BAUMGARDNER,[c] AARON BANSEMER,[b] STEVEN J. ABEL,[d] JONATHAN CROSIER,[e] JEFF FRENCH,[f] PHIL ROSENBERG,[g] ALEXEI KOROLEV,[h] ALFONS SCHWARZOENBOECK,[i] DELPHINE LEROY,[i] JUNSHIK UM,[a] WEI WU,[a,b] ANDREW J. HEYMSFIELD,[b] CYNTHIA TWOHY,[j] ANDREW DETWILER,[k] PAUL FIELD,[d,g] ANDREA NEUMANN,[l] RICHARD COTTON,[d] DUNCAN AXISA,[b] AND JIAYIN DONG[a]

[a] *University of Illinois at Urbana–Champaign, Urbana, Illinois*
[b] *National Center for Atmospheric Research, Boulder, Colorado*
[c] *Droplet Measurement Technologies, Boulder, Colorado*
[d] *Met Office, Exeter, United Kingdom*
[e] *University of Manchester, Manchester, United Kingdom*
[f] *University of Wyoming, Laramie, Wyoming*
[g] *University of Leeds, Leeds, United Kingdom*
[h] *Environment and Climate Change Canada, Downsview, Ontario, Canada*
[i] *Laboratoire de Météorologie Physique, CNRS/Université Blaise Pascal, Aubière, France*
[j] *NorthWest Research Associates, Redmond, Washington*
[k] *South Dakota Schools of Mines and Technology, Rapid City, South Dakota*
[l] *University of North Dakota, Grand Forks, North Dakota*

ABSTRACT

In situ observations of cloud properties made by airborne probes play a critical role in ice cloud research through their role in process studies, parameterization development, and evaluation of simulations and remote sensing retrievals. To determine how cloud properties vary with environmental conditions, in situ data collected during different field projects processed by different groups must be used. However, because of the diverse algorithms and codes that are used to process measurements, it can be challenging to compare the results. Therefore it is vital to understand both the limitations of specific probes and uncertainties introduced by processing algorithms. Since there is currently no universally accepted framework regarding how in situ measurements should be processed, there is a need for a general reference that describes the most commonly applied algorithms along with their strengths and weaknesses. Methods used to process data from bulk water probes, single-particle light-scattering spectrometers and cloud-imaging probes are reviewed herein, with emphasis on measurements of the ice phase. Particular attention is paid to how uncertainties, caveats, and assumptions in processing algorithms affect derived products since there is currently no consensus on the optimal way of analyzing data. Recommendations for improving the analysis and interpretation of in situ data include the following: establishment of a common reference library of individual processing algorithms, better documentation of assumptions used in these algorithms, development and maintenance of sustainable community software for processing in situ observations, and more studies that compare different algorithms with the same benchmark datasets.

1. Introduction

Ice clouds cover ~30% of Earth (Wylie et al. 2005; Stubenrauch et al. 2006) and make substantial contributions to radiative heating in the troposphere (Ramaswamy and Ramanathan 1989). To represent cloud feedbacks in climate models, the effect of ice clouds on longwave and

[m] Current affiliation: Cooperative Institute for Mesoscale Meteorological Studies, School of Meteorology, University of Oklahoma, Norman, Oklahoma.

Corresponding author: Prof. Greg McFarquhar, mcfarq@ou.edu

DOI: 10.1175/AMSMONOGRAPHS-D-16-0007.1

© 2017 American Meteorological Society. For information regarding reuse of this content and general copyright information, consult the AMS Copyright Policy (www.ametsoc.org/PUBSReuseLicenses).

Brought to you by University of Alabama in Huntsville | Unauthenticated | Downloaded 02/05/25 05:57 PM UTC

shortwave radiation must be quantified (e.g., Ardanuy et al. 1991). Ice microphysical processes also affect the evolution of weather phenomena through impacts on latent heating, which in turn drives the system dynamics. For example, downdrafts near the melting level in mesoscale convective systems are forced by cooling associated with sublimation and melting (e.g., Grim et al. 2009), and the release of latent cooling at the melting layer feeds back on the dynamics of winter storms (e.g., Szeto and Stewart 1997). Also, the ice phase is crucial to the hydrological cycle where most of the time that rain is observed at the ground it is the result of snow that has melted higher up (Field and Heymsfield 2015).

To improve the representation of cloud microphysical processes in models, their microphysical properties must be better characterized because they determine the ice cloud impact on radiative (e.g., Ackerman et al. 1988; Macke et al. 1996) and latent heating (e.g., Heymsfield and Miloshevich 1991). An extensive array of parameters that describes cloud microphysical properties can be derived from microphysical measurements, including single-particle characteristics (e.g., size, shape, mass or effective density, and phase), particle distribution functions [e.g., number distribution functions in terms of maximum diameter $N(D_{\max})$], and bulk properties (e.g., extinction β, total mass content w_t, median mass diameter D_m, effective radius r_e, and radar reflectivity factor Z_e). Note that all symbols are defined in appendix A.

Past studies have used in situ observations to develop parameterizations of these microphysical properties. In particular, parameterizations of $N(D_{\max})$ (e.g., Heymsfield and Platt 1984; McFarquhar and Heymsfield 1997; Ivanova et al. 2001; Boudala et al. 2002; Field and Heymsfield 2003; Field et al. 2007; McFarquhar et al. 2007a), w_t (Heymsfield and McFarquhar 2002; Schiller et al. 2008; Krämer et al. 2016), mass–dimensional relations used to estimate w_t (Locatelli and Hobbs 1974; Brown and Francis 1995; Heymsfield et al. 2002a,b, 2004, 2010; Baker and Lawson 2006; Heymsfield 2007; Fontaine et al. 2014; Leroy et al. 2017), and single-particle light-scattering properties (Kristjansson et al. 2000; McFarquhar et al. 2002; Nasiri et al. 2002; Baum et al. 2005a,b, 2007, 2011; Baran 2012; van Diedenhoven et al. 2014) have been developed. In addition, parameterizations of effective radius (Fu 1996; McFarquhar 2001; McFarquhar et al. 2003; Boudala et al. 2006; Liou et al. 2008; Mitchell et al. 2011a; Schumann et al. 2011) and terminal velocity (Heymsfield et al. 2002b; Heymsfield 2003; Schmitt and Heymsfield 2009; Mitchell et al. 2011b) that rely on measured size and shape distributions have been derived. While such parameterizations are appropriate for schemes that predict bulk moments of predefined ice categories (e.g., Dudhia 1989; Rotstayn 1997; Reisner et al. 1998; Gilmore et al. 2004; Ferrier 1994; Walko et al. 1995; Meyers et al. 1997; Straka and Mansell 2005; Milbrandt and Yau 2005; Thompson et al. 2004, 2008), there is a new generation of models (e.g., Sulia and Harrington 2011; Harrington et al. 2013a,b; Morrison and Milbrandt 2015; Morrison et al. 2015) that explicitly predict particle properties that require information about single particles in addition to bulk properties. In situ data are also needed to verify and develop retrievals from radar and lidar (e.g., Atlas et al. 1995; Donovan and van Lammeren 2001; Platnick et al. 2001; Hobbs et al. 2001; Frisch et al. 2002; Mace et al. 2002; Deng and Mace 2006; Shupe et al. 2005; Hogan et al. 2006; Delanoë et al. 2007; Austin et al. 2009; Kulie and Bennartz 2009; Deng et al. 2013).

In situ measurements of ice cloud properties are thus needed in a variety of cloud types and geographic regimes. Although in situ measurements are commonly treated as "ground truth," they are subject to errors and biases. Thus, uncertainties in derived parameters must be established to understand the consequences for associated model and retrieval studies. Knowledge of uncertainties is also needed for the development and application of stochastic parameterization schemes (e.g., McFarquhar et al. 2015). It is difficult to specify a priori the acceptable uncertainty in a measured or derived quantity that is application dependent. For example, studies of secondary ice production (e.g., Field et al. 2017, chapter 7) might find an error of a factor of 2 in number concentration acceptable, whereas radiative flux calculations, which require accuracies of ±5% for climate studies (Vogelmann and Ackerman 1995), require smaller uncertainties. Other chapters in this monograph better define acceptable levels of uncertainty for different phenomena.

Measurements from in situ probes are typically quoted in units of number of particles per unit volume (e.g., concentration) or mass per unit volume (e.g., mass content). However, care must be taken when comparing against output from numerical models where concentrations and mass contents are typically represented in terms of a unit mass of air (e.g., Isaac and Schmidt 2009). Thus, in situ measured quantities must be divided by the air density when comparing against modeled quantities. Caution must also be used when comparing in situ measurements to remotely sensed retrievals or numerical model output because of differences in averaging lengths or sample volumes. For example, Fig. 4.11 of Isaac and Schmidt (2009) demonstrates how average in situ measured liquid mass contents change with averaging scale, and Wu et al. (2016) demonstrate the impact of averaging scale on the variability of the sampled size distributions. Finlon et al. (2016) define what

Brought to you by University of Alabama in Huntsville | Unauthenticated | Downloaded 02/05/25 05:57 PM UTC

TABLE 11-1. Previous workshops that have concentrated on instrumentation issues associated with the measurement of cloud microphysical properties.

Workshop	Year	Sponsor	Reference
Cloud Measurement Symposium	1982		Baumgardner and Dye (1982; 1983)
Workshop on Processing 2D data	1984		Heymsfield and Baumgardner (1985)
Workshop on Airborne Instrumentation	1988		Cooper and Baumgardner (1988)
EUFAR Expert Groups on liquid- and ice-phase measurements	2002	EUFAR	
Advances in Airborne Instrumentation for Measuring Aerosol, Cloud, Radiation and Atmospheric State Parameters Workshop	2008	DOE ARM Aerial Facility (AAF)	McFarquhar et al. (2011a)
Workshop on In Situ Airborne Instrumentation: Addressing and Solving Measurement Problems in Ice Clouds	2010		Baumgardner et al. (2012)
Workshop on Measurement Problems in Ice Clouds	2013		
Workshop on Data Analysis and Presentation of Cloud Microphysical Measurements	2014	NSF and NASA	
Workshop on Data Processing, Analysis and Presentation Software	2016	EUFAR and ICCP	

represents collocation between in situ and remote sensing data: they suggest in situ data should be between 250 and 500 m horizontally, less than 25 m in altitude, and within 5 s of collocated remotely sensed data. These discrepancies between in situ and other measurements should be taken into account when interpreting the results of processing algorithms presented in this chapter.

Multiple probes are needed to measure microphysical properties given the wide range of particle shapes, sizes, and concentrations that exist in nature. Thus, it is critical to understand the strengths, limitations, uncertainties, and caveats associated with the derivation of ice properties from different probes. Two other chapters in this monograph are dedicated to these issues. Baumgardner et al. (2017, chapter 9) discusses instrumental problems, concentrating on measurement principles, limitations, and uncertainties. Korolev et al. (2017, chapter 5) examines issues related to mixed-phase clouds, concentrating on additional complications in measurements and related processing that arise when liquid and ice phases coexist. This current chapter concentrates on an additional source of uncertainty that has not received as much attention, namely, that introduced by algorithms used to process data. Such algorithms play a critical role in determining data quality. This chapter documents the fundamental principles of algorithms used to process data from three classes of probes that are frequently used to measure cloud microphysical properties: bulk water, forward-scattering, and cloud-imaging probes. Although the discussion is slanted toward issues associated with derivation of ice cloud properties, it is noted that these algorithms apply to both liquid water and ice clouds, as well as to other types of particles, such as mineral dust aerosols that can be detected by some of these sensors.

As sensors have developed and evolved, so have the methodologies for processing, evaluating, and interpreting the data. Although several prior studies have compared measurements from different probes or versions of probes (e.g., Gayet et al. 1993; Larsen et al. 1998; Davis et al. 2007), fewer studies have systematically compared or assessed the algorithms used to process probe data or determined the optimum processing methods and the corresponding uncertainties in derived products. For example, most of the previous workshops listed in Table 11-1 have been dedicated to problems associated with the measurement of cloud properties, but until recently only the 1984 Workshop on Processing 2D data (Heymsfield and Baumgardner 1985) concentrated on techniques used to analyze or process measurements. With this in mind, workshops on Data Analysis and Presentation of Cloud Microphysical Measurements at the Massachusetts Institute of Technology (MIT) in 2014 and on Data Processing, Analysis and Presentation Software at the University of Manchester in 2016 were conducted. Many commonly used processing and analysis methodologies were compared by processing several observationally and synthetically generated datasets, representative of a range of cloud conditions. This article reviews and extends the proceedings and findings of these workshops. In particular, the basis and uncertainties in algorithms for bulk water, forward-scattering, and cloud-imaging probes are described, different algorithms designed to process data are compared, and future steps to improve processing of cloud microphysical data are suggested.

2. Probes measuring bulk water mass content

Chapter 9 (Baumgardner et al. 2017) describes the operating principle of heated sensor elements, their basis for detection and derivation of water mass content, measurement limitations, and uncertainties. In this section, the fundamental method of processing data from heated sensors based on thermodynamic principles is

Brought to you by University of Alabama in Huntsville | Unauthenticated | Downloaded 02/05/25 05:57 PM UTC

reviewed, focusing on the Nevzorov and King probes. In addition, algorithms deriving w_t from evaporator probes, namely, the Counterflow Virtual Impactor (CVI; note that all acronyms are defined in appendix B) and Cloud Spectrometer and Impactor Probe (CSI), are reviewed. Processing algorithms for other bulk total water probes—such as the Scientific Engineering Applications (SEA) hot-wire Robust probe (Lilie et al. 2004); the SEA Isokinetic Evaporator Probe (IKP2), specifically designed for measuring high w_t at high speeds (Davison et al. 2009); and the Particle Volume Monitor (PVM; Gerber et al. 1994)—are not discussed because there are not multiple algorithms for processing these data, and when there are, there is minimal variation between algorithms.

Although the King probe was designed to measure liquid water content w_l, its sensor does respond to ice (e.g., Cober et al. 2001) but in an unpredictable manner. Processing algorithms for the King and Nevzorov probes have many common features, and both are discussed in this chapter. While the King probe has a single sensor for sampling liquid, the Nevzorov probe has two sensors: one for measuring w_l and another for measuring w_t. The determination of w_l from the King and Nevzorov probes is discussed here because the processing concepts assist in understanding how w_t is derived and because w_l is needed for a characterization of mixed-phase clouds.

The King and Nevzorov probes are referred to as "first principle" instruments because the heat lost from the sensor through the transfer of energy via radiation, conduction, convection, and evaporation of droplets can be directly calculated based on thermodynamic principles. The first two components are usually ignored because their contribution to the total power is negligible compared to the other two terms. Thus, the power W required to keep the wire at a constant temperature T_w is given by

$$W = ldVw_l[L_v + c(T_w - T_a)] + P_D, \qquad (11\text{-}1)$$

where the first term (wet term) is the heat required to warm the droplets from the ambient temperature T_a to T_w and evaporate them, and the second term (P_D dry term) is the heat transferred to the cooler air moving past the wire. In Eq. (11-1), l and d are the length and diameter of the cylinder, V is the velocity of air passing over the sensor, L_v is the latent heat of vaporization, and c is the specific heat of liquid water. To extract w_l, the energy lost to the air P_D must be subtracted from the total energy consumed. This procedure is implemented differently in the King and Nevzorov probes.

a. Dry term estimation for King probe analysis

The King probe (King et al. 1978) consists of a thin copper wire wound on a hollow 1.5-mm-diameter cylinder. It estimates w_l through the electrical current required to maintain the sensor at a constant temperature (Baumgardner et al. 2017, chapter 9). This is an improvement over its predecessor, the Johnson–William probe, which heated a 0.5-mm-diameter wire with an electrical current as part of a bridge circuit at a constant current but not constant temperature.

King et al. (1978) suggested that the dry term P_D could be parameterized by $P_D = b'(T_w - T_a)\mathrm{Re}^x$, where Re is the Reynold's number and the x and b' parameters are established in either a wind tunnel or from flight measurements. Recent investigations at NCAR and the University of Wyoming (A. Rodi 2016, personal communication). have established that the Zukauskas and Ziugzda (1985) method gives a better representation of P_D in terms of Re and the Prandtl number evaluated at the film and wire temperatures T_f and T_w, respectively.

The T_f, T_w, T_a, V, and the air pressure P must be known to determine the dry term P_D. The temperature in a region near the sensor is T_f and is assumed to be the average of T_w and T_a. This however, remains an untested assumption. In addition, there are major uncertainties in determining T_w and V since V is usually not identical to the velocity of the aircraft because of airflow distortions in the sensor's vicinity (Baumgardner et al. 2017, chapter 9).

There are two approaches to estimating the dry-air term. The constant altitude method (CAM) is preferably implemented on a cloud-by-cloud basis. The power is measured prior to and after cloud penetration and averaged to obtain the dry-air term for one cloud pass. This approach makes the following assumptions: 1) the presence of cloud can be detected with another instrument or through some thresholding technique to use the hot-wire sensor as a cloud detector, and 2) T_a, P, and V do not vary significantly (typically $<10\%$) inside or outside the cloud.

The optimum parameterization method (OPM) requires an estimate of T_f and a factor V_f, to correct the aircraft velocity to the velocity over the sensor. The velocity correction factor is assumed constant for a particular mounting location. This approach also assumes that there is a way to detect clouds so that only cloud-free measurements are used in the calculation. The parameter estimates can be made over a whole project, over one flight, or as a function of altitude. The following steps obtain the optimum values: 1) select a value for T_f and V_f; 2) compute P_D for every measured data point; 3) calculate an error metric between the measured power P_m and P_D, for example, $\Sigma(P_m - P_D)^2$; 4) check if the error is above a threshold value; and if it is, 5) adjust T_f, and V_f and return to step 1.

Brought to you by University of Alabama in Huntsville | Unauthenticated | Downloaded 02/05/25 05:57 PM UTC

For the MIT workshop, the OPM and CAM methods were applied to an unprocessed raw dataset supplied by the NCAR Research Applications Laboratory (RAL). The measurements were made with a Particle Measuring Systems (PMS) LWC hot-wire sensor mounted on the Aerocommander aircraft flown during the 2011 Cloud–Aerosol Interaction and Precipitation Enhancement Experiment (CAIPEEX) over the Indian Ocean. The clouds sampled were all liquid water with no ice. Figure 11-1 shows w_l derived from the raw data using the CAM and OPM methods and their average, compared with the results from processing performed at RAL using a constant wire temperature and dry-air term parameterized by the Reynolds and Prandtl numbers (Zukauskas and Ziugzda 1985). The differences between the two techniques are negligible.

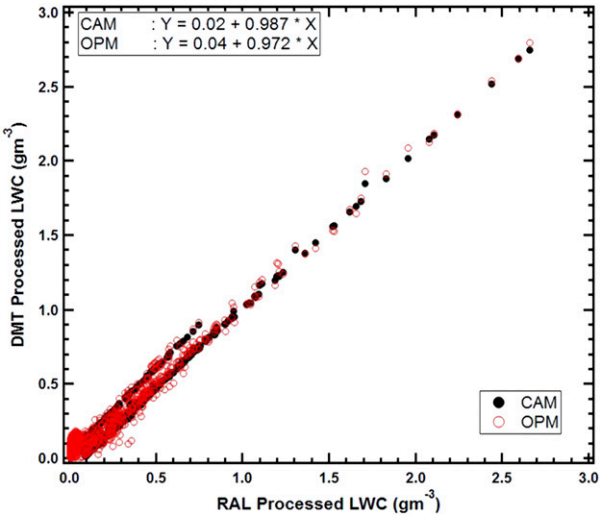

FIG. 11-1. Mass content w_l derived by DMT, using CAM and OPM as a function of w_l derived using a constant wire temperature and dry-air term parameterization by the Reynolds and Prandtl numbers (Zukauskas and Ziugzda 1985) for measurements made with a PMS LWC hot-wire sensor mounted on the Aerocommander aircraft during the 2011 CAIPEEX over the Indian Ocean. The clouds sampled were all liquid water with no ice.

b. *Nevzorov probe analyses*

As discussed in Baumgardner et al. (2017, chapter 9), the Nevzorov hot-wire probe (Korolev et al. 1998a, 2013a) consists of a heated cone mounted on a moveable vane to measure w_t and a heated wire wound onto a copper rod to measure w_l, with $w_t = w_l + w_i$. Liquid droplets impacting either sensor should evaporate fully, but ice particles tend to break up and fall away from the liquid water sensor, although a residual signal from these ice particles is often observed (Korolev et al. 1998a). As the heated sensors are exposed to the airflow, forced convective cooling adds to the power requirement to melt and evaporate cloud particles. The cooling depends on the aircraft attitude and environmental conditions. A reference sensor partially compensates for this convective cooling and enables removal of most of the dry-air heat-loss term. Assuming $w_l = 0$, the ice water content (w_i) in ice clouds can be calculated following

$$w_i = \frac{P_C - KP_R}{VSL^*}, \tag{11-2}$$

where P_C and P_R are the collector and reference sensor power, S is the sensor sample area, L^* is the energy required to melt and evaporate measured hydrometeors, and K is the ratio of the collector to reference power that is dissipated in cloud-free air representing the dry-air heat loss term. The lack of full compensation for this term by the reference sensor leads to a variation in K during a flight and hence a ''baseline drift'' of the calculated w_i. Korolev et al. (1998a) and Abel et al. (2014) show that K is dependent on V and environmental conditions. The probe precision in w_i can reach $\pm 0.002\,\mathrm{g\,m^{-3}}$, providing that the baseline drift is removed by adequately capturing how K varies over the flight (Abel et al. 2014). In the event $w_l \neq 0$, more complications arise because the liquid sensor partially responds to ice, so even subtracting w_l from w_t gives a larger error in the estimated w_i.

Nevzorov data from three flights were processed for the 2014 workshop by two groups that were not publicly identified, henceforth represented as G1 and G2. The data were from two flights of the University of North Dakota Citation II aircraft, one within a trailing stratiform region of a mesoscale convective system and the other from a flight in supercooled convective showers. The third dataset was from a flight in midlatitude cirrus on the FAAM BAe-146 research aircraft. Both groups characterized the baseline drift of the probe by looking at how K varied as a function of indicated airspeed (IAS) and P. The groups, however, used different functional forms. G1 calculated $\Delta K = a_1\Delta(1/\mathrm{IAS}) + a_2\Delta\log_{10}(P)$ and G2 calculated K as $K = b_1\mathrm{IAS} + b_2P + b_3$. The coefficients a_1, a_2, b_1, b_2, and b_3 were calculated on a flight-by-flight basis using cloud-free data points.

Figure 11-2 shows P_C/P_R, K (i.e., the baseline), and w_t derived by G1 and G2 denoted $w_{t\mathrm{G1}}$ and $w_{t\mathrm{G2}}$, respectively. The different parameterizations of K capture similar trends in the baseline drift for each flight, with small offsets on two of the flights. The impact of these offsets leads to systematic biases in the calculation of w_t, with the largest mean difference $w_{t\mathrm{G1}} - w_{t\mathrm{G2}}$ being as high as $-0.011\,\mathrm{g\,m^{-3}}$ for the convective cloud flight. An indication of the agreement between data processed by the two groups is given by the $\pm 1\sigma$ values of $w_{t\mathrm{G1}} - w_{t\mathrm{G2}}$,

Brought to you by University of Alabama in Huntsville | Unauthenticated | Downloaded 02/05/25 05:57 PM UTC

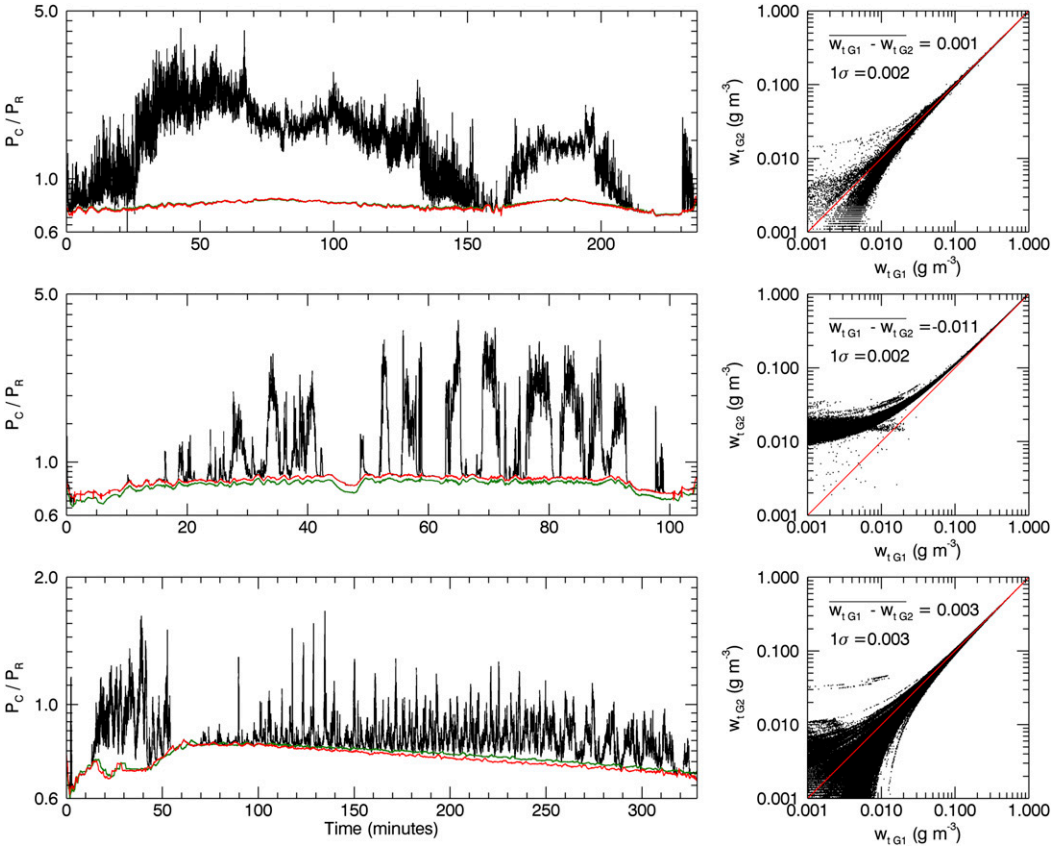

FIG. 11-2. (left) Measured P_C/P_R (black) from Nevzorov w_t sensor. Cases include data from (top) a trailing stratiform region of a mesoscale convective system collected using the University of North Dakota (UND) Citation, (middle) supercooled convective showers collected using the UND Citation, and (bottom) midlatitude cirrus collected using the FAAM BAe-146 research aircraft. K parameter calculated by G1 and G2 shown in red and green, respectively. (right) Comparison of the calculated w_t from G1 and G2. The red line is the 1:1 line.

which are ± 0.002, ± 0.002, and $\pm 0.003\,\mathrm{g\,m^{-3}}$ for the three flights.

c. CVI and CSI analysis

The CVI/CSI condensed water measurement is based on water vapor measured directly after hydrometeor evaporation or sublimation in the inlet of the instrument (Noone et al. 1988; Twohy et al. 1997). As described in chapter 9 (Baumgardner et al. 2017), the water vapor from evaporated cloud droplets or ice crystals is measured downstream, typically by a tunable diode laser (TDL) hygrometer. Most accurate results are obtained when the hygrometer is calibrated for the full range of pressures and water vapor contents that will be encountered, generating a nonlinear coefficient matrix that is a function of both vapor concentration and pressure. The basic processing involves applying the calibration to the measured vapor content and dividing by an enhancement factor. The enhancement factor is calculated as the volumetric flow of air ingested by the CVI/CSI probe tip (airspeed multiplied by cross-sectional area) divided by the total volumetric flow of air inside the CVI inlet (sum of all downstream flow rates that are continuously monitored). The root-sum-square uncertainty using a TDL sensor is estimated as $\pm 11\%$ for $0.05 < w_t < 1.0\,\mathrm{g\,m^3}$, $\pm 15\%$ at $0.05\,\mathrm{g\,m^3}$, and $\pm 23\%$ for $w_t \leq 0.025\,\mathrm{g\,m^3}$ (Heymsfield et al. 2006; Davis et al. 2007).

Special processing can be applied for additional accuracy. Outside cloud, the measured w_t should be zero, since ambient air is prevented from entering the inlet by a counterflow, and dry gas is recirculated throughout the internal system. Depending on the response of the water vapor sensor to changing pressure, a small baseline offset may remain after calibration. This precloud-entry baseline offset may be removed from in-cloud data before the enhancement factor is applied. At high w_t, water vapor inside the inlet may saturate or exceed the capabilities of the sensor, leading to saturation flatlining of the signal. This problem can be minimized by

Brought to you by University of Alabama in Huntsville | Unauthenticated | Downloaded 02/05/25 05:57 PM UTC

adjusting flow rates during flight to decrease the enhancement factor. Hysteresis may also occur through incomplete evaporation or water vapor adhering to internal surfaces, which results in water vapor being measured subsequent to cloud sampling. For sharper time resolution, the water vapor in the postcloud hysteresis tail can be added back to the in-cloud signal, using cloud exit time determined from other cloud sensors.

3. Light-scattering spectrometers

Chapter 9 (Baumgardner et al. 2017) describes the operating principle of light-scattering probes. These spectrometers were originally developed to measure the size distributions of liquid water and supercooled water droplets, but with appropriate modifications in processing algorithms can also provide information about $N(D_{\max})$ in ice clouds. From the measured $N(D_{\max})$, other properties such as total number concentration, effective radius and water content can be derived. In this section, the fundamental methods of processing data from light-scattering spectrometers are discussed, and comparisons between different algorithms are made.

The discussion centers around algorithms used to process data from probes that scatter light in the forward direction. These instruments include the Forward Scattering Spectrometer Probe (FSSP), a legacy probe originally manufactured by PMS and Particle Metrics Incorporated (PMI); the revised signal-processing package (SPP-100), an FSSP with electronics upgraded to eliminate dead time and manufactured by DMT; the Cloud Droplet Probe (CDP), Cloud and Aerosol Spectrometer (CAS), and CDP-2 with upgraded electronics, all manufactured by DMT; the Fast FSSP (FFSSP), an FSSP retrofit with upgraded (fast) electronics and probe tips, and the Fast Cloud Droplet Probe (FCDP), which is a unique design with fast electronics, both of which are manufactured by SPEC. Probes that measure scattering in multiple directions [e.g., the small ice particle detector (SID) or polar nephelometers], in the backward direction [e.g., Backscatter Cloud Probe (BCP)] or including polarization [e.g., Cloud and Aerosol Spectrometer with Polarization (CAS-POL), Backscatter Cloud Probe with Polarization Detection (BCPD), or the Cloud Particle Spectrometer with Polarization Detection (CPSPD)] are not discussed because there is more variation in algorithms used to process data from these spectrometers. Although the basics of algorithms are identical for liquid water and ice particles, there are additional uncertainties in sizing nonspherical ice particles described at the end of this section. Beyond the sizing of nonspherical particles and the inescapable sampling uncertainty (Hallett 2003), there are two other major sources of error in calculating the number concentration: coincidence and shattering.

a. *Adjustments for coincidence*

Coincidence occurs when more than one particle is within the sensor's laser beam. The impact of this event depends on the relative position of the particles. Particles coincident in the qualified sample area (SA_Q) are counted as a single, oversized particle. But, when one particle is in the SA_Q and the other outside SA_Q, but in the extended sample area [SA_E; i.e., particles detected by the sizer that transit outside the SA_Q; see chapter 9 (Baumgardner et al. 2017) and Fig. 2 in Lance (2012) for the definitions of SA_Q and SA_E and more details on the operation of forward-scattering probes], the particles will be missized and possibly even rejected depending on their relative sizes (Baumgardner et al. 1985; Brenguier and Amodei 1989; Brenguier 1989; Brenguier et al. 1994; Cooper 1988; Lance 2012). Lance (2012) describes an optical modification to a CDP that places an 800-μm-diameter pinhole in front of the sizing detector. This reduces particle coincidence in the SA_E because otherwise unqualified drops that transit outside the SA_Q can still be detected by the sizer. Nevertheless, even with a SA_E of 2.7 mm^2 in the modified CDP (Lance 2012) and a beamwidth of 200 μm, a sample volume of 0.54 mm^3 means more than one particle will be detected in the SA_E for concentrations greater than 1850 cm^{-3}, assuming a uniform spatial distribution of particles. However, as particles are randomly distributed or perhaps clustered (e.g., Paluch and Baumgardner 1989; Baker 1992; Pinsky and Khain 1997; Davis et al. 1999; Kostinski and Jameson 1997, 2000), the data still need to be adjusted to account for the effect of coincidence.

Previously these adjustments have been called corrections; however, the term ''corrections'' suggests that there is a priori knowledge of the actual size distribution, which is typically not the case. Thus, the term ''adjustments'' is used henceforth. Note that it is especially important to adjust for coincidence when very high particle concentrations are present or at lower concentrations when processing data from unmodified probes (e.g., an SA_E of 20.5 mm^2 for the unmodified CDP suggests more than one particle in the sample volume for concentrations greater than 243 cm^{-3}).

Coincidence events cannot be avoided, but statistical or empirical adjustments, as well as alternate methods of particle counting, are possible. Statistical adjustments assume that particles are randomly distributed in space and that the probability of a particle in the beam is given by $1 - e^{-\lambda\tau}$ where τ is the average transit time of a particle in the depth of field (DOF) and λ is the particle

Brought to you by University of Alabama in Huntsville | Unauthenticated | Downloaded 02/05/25 05:57 PM UTC

detection rate, where $\lambda = N_a A_{\mathrm{DOF}} V$ (Baumgardner et al. 1985) with N_a the ambient particle number concentration, A_{DOF} the DOF area and V the velocity of the air passing over the sensor. The relationship between the measured number concentration N_m and N_a is approximated by Baumgardner et al. (1985) as

$$N_m = N_a(T - \tau_d)e^{-\lambda\tau}/T, \tag{11-3}$$

where T is the sampling period and τ_d is the cumulative dead time during the time of the sample interval. The dead time corresponds to the time required to reset the electronics after a particle has left the beam. During this reset period the probe does not detect particles. This nonlinear relationship can be solved iteratively for N_a.

Another adjustment method requires either a direct measurement or estimate of the probe activity α. Activity is the fraction of the sampling interval that the instrument is processing a particle, including the time a particle has been detected in the beam, either within or outside the DOF, and the dead time. The dead time is only relevant for the legacy FSSPs manufactured by PMS and PMI, and SID-type instruments that have a fixed dead time after each particle. Legacy FSSPs that have been modified with the DMT SPP-100 electronics do not suffer from dead time. The adjustment factor C_f is given by

$$C_f = (1 - m\alpha)^{-1}, \tag{11-4}$$

where m is a probe-dependent adjustment factor and

$$N_a = C_f N_m. \tag{11-5}$$

Original manufacturer recommendations suggest a value of m between 0.7 and 0.8. However, simulations have shown that this may vary from 0.6 to 0.8 (Baumgardner et al. 1985), and values as low as 0.54 (Cerni 1983) can be found in the literature. Brenguier (1989) suggests the value lies between 0.5 and 0.8. More studies are needed to establish a value for m that may be probe dependent. For the CDP and CAS, the activity can be approximated by

$$\alpha = n_m T_s / T, \tag{11-6}$$

where n_m is the number of particles counted in sample interval T, and T_s is the average transit time; however, a value for m has yet to be derived for these probes.

A similar approach uses the measured activity but takes into account probe-specific parameters such as laboratory-measured electronic delay times including dead time and time response of amplifiers, beam diameter, and DOF (Dye and Baumgardner 1984). This statistical approach models the behavior of the probe assuming droplets passing through the sample volume are uniformly distributed in space with a constant mean density (Brenguier and Amodei 1989). The algorithm computes an actual concentration by estimating the probability of a coincidence event based on the activity and other probe parameters. An equivalent m can be determined using Eqs. (11-4) and (11-5), but the equivalent m will vary such that it asymptotically approaches 1 with increasing droplet concentration. The value of m depends on probe-specific parameters and on the transit time of individual particles (Brenguier 1989). No simple functional relationship exists between m and α. For the data presented by Brenguier (1989), the minimum m was less than 0.6 at low activities but exceeded 0.8 for higher activities.

Examples of the above two methodologies are compared for data collected by an FSSP on the University of Wyoming King Air in convective clouds with droplet concentrations in excess of $1000\,\mathrm{cm}^{-3}$ during the Convective Precipitation Experiment (COPE) in 2013 over southwest England. Data from 3 separate days were selected for analysis from penetrations where no significant precipitation-sized particles were detected by the imaging probes. Figure 11-3a shows three coincidence-adjusted estimates of droplet concentration as a function of N_m. The red and blue circles show the coincidence-adjusted concentrations using a constant m of 0.54 and 0.71, respectively, and green circles show the concentrations adjusted using the method of Brenguier and Amodei (1989). The solid line indicates the 1:1 line and dashed lines show 20%, 50%, and 100% adjustments to N_m. For $N_m < 200\,\mathrm{cm}^{-3}$, coincidence adjustments are less than 20%. For $200 < N_m < 400\,\mathrm{cm}^{-3}$, coincidence adjustments may be as large as 75% with differences depending on the chosen value for m. In this range of N_m, differences between adjusted concentrations are small when comparing the Brenguier and Amodei (1989) method with the method of a fixed m equal to 0.71. For $N_m > 500\,\mathrm{cm}^{-3}$, coincidence adjustments may exceed 100% and differences between using a fixed m of 0.71 and the statistical model of Brenguier and Amodei (1989) approach 20%.

The same three coincidence-adjusted FSSP concentrations are shown in Fig. 11-3b and plotted as a function of N_m from a CDP. The CDP had been modified with the "pinhole" to reduce impacts of coincidence (Lance et al. 2010; Lance 2012) and the sample volume was measured by the probe manufacturer. Coincidence-adjusted concentrations from the FSSP agree to within 20% of measured CDP concentrations for $N_m < \sim 500\,\mathrm{cm}^{-3}$. For larger N_m, coincidence-adjusted concentrations for the FSSP using a fixed m of 0.71 or the statistical method

Brought to you by University of Alabama in Huntsville | Unauthenticated | Downloaded 02/05/25 05:57 PM UTC

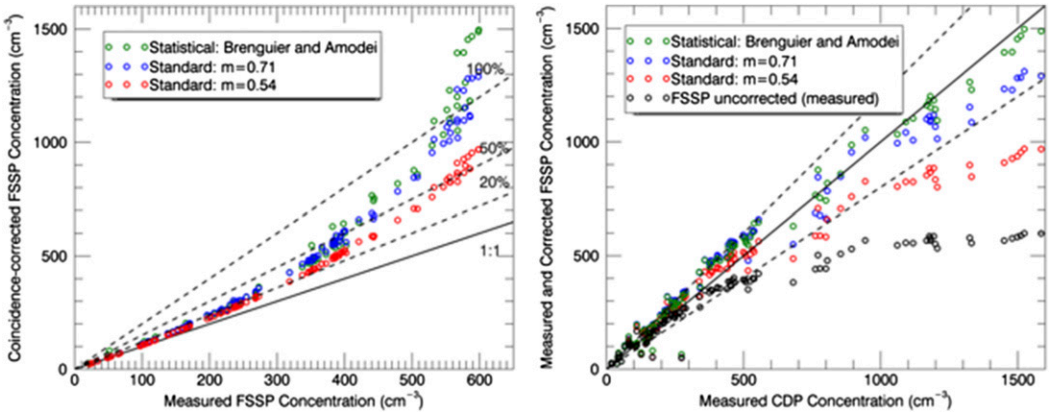

FIG. 11-3. (left) Activity-based coincidence-corrected concentration as a function of raw (measured) concentration from the FSSP for values of fixed m of 0.54 (red) and 0.71 (blue) and for the statistical method of Brenguier and Amodei (green) for data collected during 2013 COPE over southwest England using the University of Wyoming King Air for 3–4-min penetrations on 3 days during periods that did not appear to contain any precipitation-sized particles. (right) Activity-based coincidence-corrected concentrations from the FSSP for the same dataset shown in (left), but compared to measured concentrations from a CDP on the same aircraft.

of Brenguier and Amodei (1989) also agree to within 20% of the CDP measurements, but the lower value of fixed m (0.54) predicts significantly lower concentration compared to those measured by the CDP.

Instruments that measure the individual particle-by-particle (PbP) interarrival times (i.e., the FCDP, FFSSP, CDP-2, and CPSPD) allow a precise estimate of activity but do not avoid coincidence. For these probes, a concentration that is almost unaffected by coincidence can be derived. The standard method for calculating concentration is $N_m = n_m/SV$, where SV is the sample volume given by SAVT. An alternative definition is $N_m = n_m/\mathrm{SA}V\Sigma\tau$, where $\Sigma\tau$ is the sum of interarrival times, and SA is the appropriate sample area.

A final approach uses an inversion technique (Twomey 1977; Markowski 1987) to derive ambient size distributions (SDs) from those measured. Here the instrument's operating principles are modeled, and its response to ambient particles predicted and compared to actual measurements. Estimates of the ambient SD are adjusted until the predicted response matches that measured within a preset error. This approach has been implemented with the BCP (Beswick et al. 2014, 2015) and should be equally effective with other scattering probes when the operating characteristics have been evaluated. As physical models of scattering probes become even more robust, the utility of inversion techniques toward nudging measurements toward realistic values will become even greater.

b. Sizing

The simplest case of using a light-scattering spectrometer for sizing is for spherical water droplets. The amount of scattered light can be derived directly from Mie–Lorenz theory. Deriving sizes for ice crystals is more complex because every crystal is unique and has the potential for different alignments with respect to the laser.

However, even for the droplet case, effectively deriving particle sizes is nontrivial. Two fundamental problems exist. First, as predicted by Mie–Lorenz theory, the amount of light scattered by a particle is not a monotonic function of diameter. The peaks and troughs in the relationship are often referred to as Mie–Lorenz oscillations and their amplitude is particularly significant for droplets smaller than $\sim 15\,\mu$m [chapter 9 (Baumgardner et al. 2017) discusses the sources of this uncertainty]. The second problem is that the properties of the instruments are often not well constrained. These properties include uncertain scattering angular sizes and imperfect alignment of apertures and beam blockers, variation in illumination intensity over the sample volume, uncertain instrument sensitivity and offset, and the amount of electronic noise. These items cause smoothing of the Mie–Lorenz oscillations or broadening of the distribution (i.e., a particle-to-particle variability even for identical diameters). Because the amount of light scattered is highly nonlinear, the impacts of broadening do not cancel in the mean as they might in a linear system. For example, if a peak in the Mie–Lorenz curve occurs just below a threshold between two sizing bins, then broadening would cause a large fraction of particles at this size to jump up into the next bin. If no trough exists just above this threshold very few particles would jump down from this higher bin, and hence the impact of broadening would be to generate a bias.

Brought to you by University of Alabama in Huntsville | Unauthenticated | Downloaded 02/05/25 05:57 PM UTC

The best efforts of the community to date to perform sizing using light-scattering spectrometers involve calibrating using well-characterized particles. The calibration particles are usually spherical glass beads (e.g., Gayet 1976; Pinnick and Auvermann 1979; Cerni 1983; Dye and Baumgardner 1984), polystyrene latex nanospheres (Nagel et al. 2007), liquid water droplets from a controlled jet (Wendisch et al. 1996; Nagel et al. 2007), or in some cases ice crystal analogs. An adjustment must be made if the calibration particles are not the same material as the particles being measured; this is called a refractive index adjustment, typically referred to as a refractive index correction in the literature. The process is nontrivial because of the Mie–Lorenz oscillations. The scattered light measured by the instrument σ is expected to be a nonmonotonic function of particle size.

Some studies (see Baumgardner et al. 2017, chapter 9) have indicated that the predicted oscillations of as much as 300% between 3 and 10 μm and of up to 50% at diameters greater than 10 μm in forward-scattering probes are not well observed though the unavailability of many closely sized and narrowly distributed calibration samples limits mapping of the oscillations. However, if an instrument is calibrated using material similar to the measured particles, it may be sensible to utilize an empirical monotonic response curve that approximates the calibration points (e.g., Cotton et al. 2010; Lance et al. 2010).

The problem with using an empirical monotonic response curve is that if an instrument is responding to Mie–Lorenz oscillations, then artifacts will be created, such as false peaks and troughs. Further, it is not obvious how to perform refractive index corrections when the calibration samples are a different composition than the in situ samples. To attempt to counter these issues, Rosenberg et al. (2012) recommends the calibration of bin boundaries in terms of the scattered light measured by the forward-scattering instrument σ (which is a linear function of instrument response) rather than the size D; then integration over ranges of D that fall in each σ bin give each bin a mean diameter and effective width rather than two bin edges. The advantages of this approach are that σ can be a nonmonotonic function of D (which could, for example be based on Mie–Lorenz theory) and uncertainties from the calibration can be rigorously propagated including ambiguities from nonmonotonic $\sigma(D)$. However, this method is simply a numerical technique for refractive index correction based on a user-supplied function $\sigma(D)$. If this user-supplied function is incorrect, because the sizes and alignments of the instrument aperture and beam blocker are unknown, the method will generate artifacts. The method can be repeated with multiple versions of $\sigma(D)$ to determine the uncertainty in sizing due to the uncertainty in this function. This method does incorporate the impacts of broadening mechanisms described above; however, the way this method integrates over the range of calibration uncertainties may have a similar impact to the broadening mechanisms.

Figure 11-4 shows an example of a size distribution from a CDP in a fair-weather cumulus (taken from FAAM flight B792) and a 3–30-μm polydisperse bead sample (provided by Whitehouse Scientific) plotted using the manufacturer's specifications and using the Rosenberg et al. (2012) method. The bead sample has had its cumulative volume distribution calibrated in the range ~9–12 μm. A cumulative lognormal curve has been fit to the provided calibration points, and then subsequently converted to a number distribution. Two versions of the Rosenberg et al. (2012) method have been applied. One using σ calculated using the standard CDP light collection angular range of 4°–12°, and one using the range 1.7°–14° recommended by the manufacturer for this instrument. The difference between the two angular ranges gives an indication of how sensitive the method is to the chosen $\sigma(D)$ and how uncertainties in this function may propagate. No attempt is made to include the effect of optical misalignments because there is no indication of how large such misalignments may be. These data are presented to highlight how a size distribution can vary greatly through different processing methodologies based on seemingly sensible assumptions. With no calibration applied, there are three peaks in the cloud distribution below 20 μm and three peaks at the same diameters in the polydisperse bead distribution. The fact that these three peaks occur in the unimodal bead distribution indicates that they are likely artifacts.

With the Rosenberg method applied and based on the size of the error bars presented by this method, it would be concluded that this is a bimodal distribution and a bimodal best fit curve is shown. However, the Rosenberg method also produces two modes for the unimodal bead distribution: one at approximately the correct size and one at a larger size. This of course casts doubt on its use for in situ measurements. The additional peak could be caused by an incorrect $\sigma(D)$ (wrong scattering angular range or failure to account for misalignment); failure to account for broadening effects; or a problem with the delivery of the sample, for example, coincidence (as described in section 3c) causing particle oversizing generating an actual mode of larger aggregate particles. This example shows how difficult it is to create a methodology and validate its ability to effectively size particles within a rigorously defined uncertainty. This is due to limitations first in models of the

Brought to you by University of Alabama in Huntsville | Unauthenticated | Downloaded 02/05/25 05:57 PM UTC

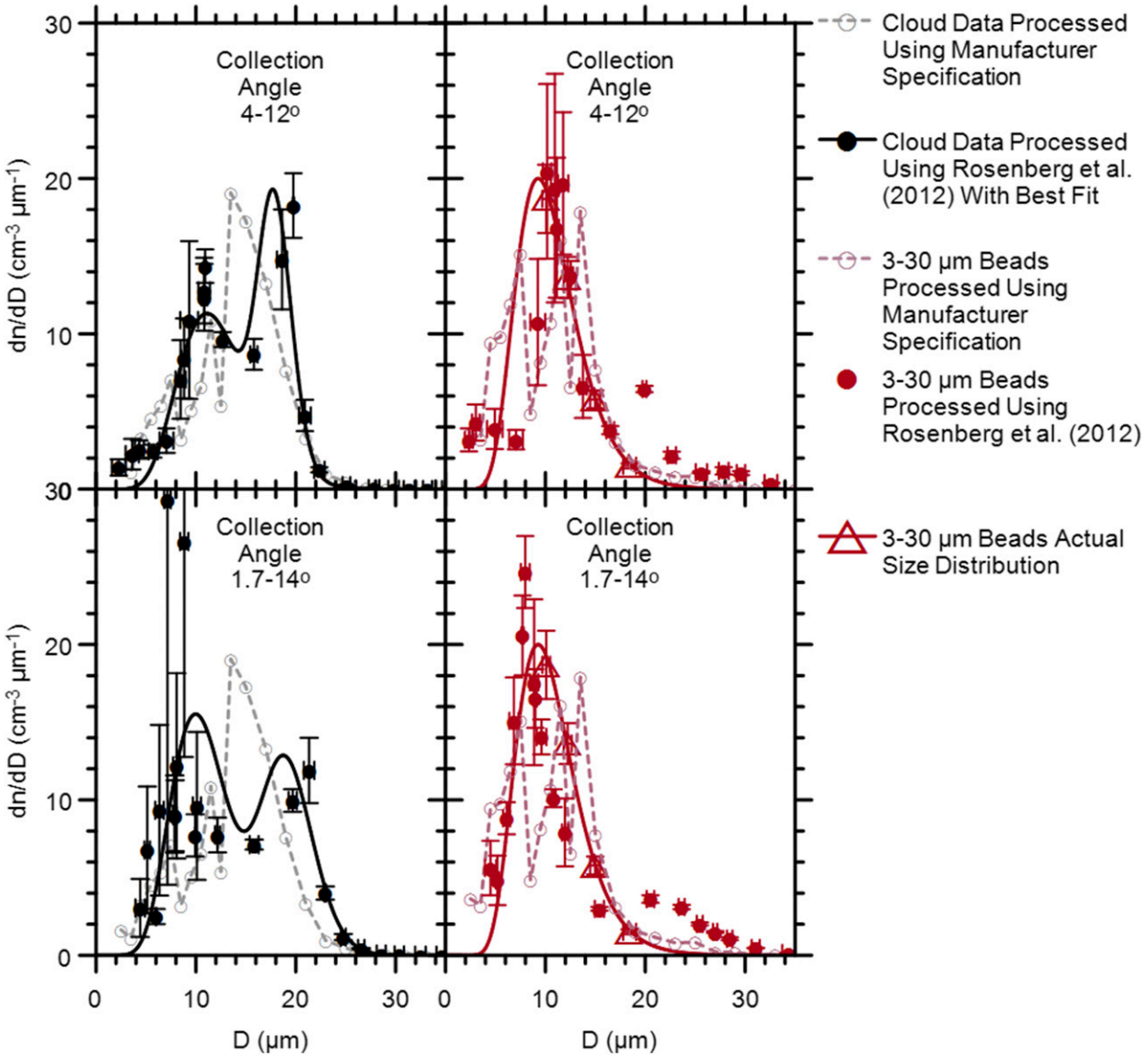

FIG. 11-4. Example of size distribution from CDP in fair-weather cumulus cloud sampled during FAAM flight B792 from 44 139 to 44 154 s after 0000 local time and from a 3–30-μm polydisperse bead sample (provided by Whitehouse Scientific) plotted using the manufacturer's specifications and using the Rosenberg et al. (2012) calibration converting from σ to D. Errors bars are 1-sigma and are dominated by the calibration errors. The manufacturer does not provide bin width uncertainties, so the data processed with the manufacturer's specifications have no error bars included.

instruments and in the ability to test methodologies against known size distributions.

A further methodology that has the potential to contribute to this field is based on an inversion technique (Twomey 1977; Markowski 1987). Here a model of the instrument is created and used to determine which estimate of reality, when passed through the model, gives the closest match to the measurements. This can be an iterative procedure or if the model can be represented by a matrix, known as a kernel, then the problem reduces to inverting the matrix. For a light-scattering spectrometer, each element of the kernel defines the probability that a particle within a particular size range will be allocated to a particular bin of the instrument. This method has the potential to account for broadening effects and has been attempted for a backscatter probe (Beswick et al. 2014). However, this method still relies upon a good model of the instrument and it is not clear that they are yet robust enough as propagation of uncertainties is difficult. There are also problems with the kernel method when dealing with poor sampling statistics.

Brought to you by University of Alabama in Huntsville | Unauthenticated | Downloaded 02/05/25 05:57 PM UTC

All of the previous discussion has been concerned with spherical particles that have well-understood light-scattering properties. There are few studies that have developed techniques to adjust SDs for the impact of coincidence, incorrect DOF, or missizing of ice crystals. Cooper (1988) illustrated an inversion technique that models the response of the FSSP to particles coincident in the beam, showing that an ambient SD can be derived from the measured SD. But, this issue needs more study to improve its accuracy, especially when concentrations are elevated. Borrmann et al. (2000) and Meyer (2013) employed *T*-matrix calculations to estimate the sizing of oblate spheroids of varying aspect ratios in order to investigate the derivation of a response function from ice crystals. The surface roughness and occlusions in ice crystals also impact their scattering properties. No systematic adjustments are currently being applied to measurements in mixed- or ice-phase clouds to account for nonspherical shapes or surface roughness partly because of uncertainties in how to represent small crystal shape (e.g., Um and McFarquhar 2011) and roughness (e.g., Collier et al. 2016; Magee et al. 2014; Zhang et al. 2016).

c. *Shattering adjustments*

It has been conclusively established that shattering of large ice crystals on the tips or protruding inlets can artificially amplify the concentrations measured by forward-scattering probes (Gardiner and Hallett 1985; Gayet et al. 1996; Field et al. 2003; Heymsfield 2007; McFarquhar et al. 2007b, 2011b; Jensen et al. 2009; Zhao et al. 2011; Febvre et al. 2012; Korolev et al. 2011, 2013b, c). In addition to the use of redesigned probe tips, the elimination of particles with short interarrival times can mitigate the presence of many artifacts. But, as discussed in section 4 as pertains to optical array probes (OAPs), the implementation of such algorithms can add uncertainties to ice crystal concentrations. Such algorithms can only be applied to the spectrometer probes that record individual particle-by-particle interarrival times.

4. Imaging probe analysis

a. *Introduction and generation of synthetic data*

Chapter 9 (Baumgardner et al. 2017) describes the operating principles of imaging probes and lists the different types in Table 9-1. Imaging probes include both OAPs that provide 10-μm or coarser-resolution images [e.g., Cloud Imaging Probe (CIP), Precipitation Imaging Probe (PIP), 2DS, HVPS-3 and the 2DC and 2DP legacy probes originally developed by PMS] as well as probes providing higher-resolution images through different operating principles (e.g., CPI, HOLODEC, PHIPS-HALO, HSI). Although analysis characterizing particle morphology and identifying particle habits are common to all imaging probes, procedures to derive $N(D_{\max})$ and total concentrations differ for OAPs and other probes because of the different manner in which sample volumes are defined. In this section, image analysis algorithms that can be applied to any class of probe are discussed. However, algorithms deriving $N(D_{\max})$ are discussed only for OAPs since such algorithms can be applied to a number of different probes and because many algorithms developed by different groups are available. The discussion does not focus on algorithms for specific probes, but rather concentrates on examining aspects of algorithms that are common to all OAPs (e.g., those manufactured by PMS, DMT, or SPEC, Inc.). Algorithms for deriving $N(D_{\max})$ from the higher-resolution imagers are not discussed here as they tend to be more specialized, applicable only to a single probe, with typically only a single algorithm developed by the instrument designer available.

To compare processing algorithms, a synthetic dataset simulating data generated by OAPs was developed at NCAR.[1] The simulation includes all major aspects of OAP performance and operation, including an optical model, an electronic delay and discretization model, particle timing information, airspeed, array clocking speed, and raw data compression and encoding. It starts with the definition of model space and characteristics of the probe to be simulated, such as the number of diodes, arm spacing, diode resolution, and diode response characteristics. Particles are then randomly placed within the three-dimensional model space. Particle sizes are determined according to a known particle SD. The particles undergo a series of simulations to reproduce the probe's response to each, including the following:

1) Optical diffraction: Knollenberg (1970) described the role of diffraction in controlling the DOF and how it varies with particle size. Korolev et al. (1991) developed a framework for simulating shadows from spherical particles based on Fresnel diffraction of an opaque disc, which is the basis for the simulations used in the model for round liquid drops.
2) Electronic response time: An OAP is composed of a linear array of photodiodes, so that the shadow level of individual diodes must be rapidly recorded at a rate proportional to the speed of the aircraft and the resolution of the instrument. The model uses the

[1] The synthetically generated datasets are publicly available at ftp://ftp.ucar.edu/pub/mmm/bansemer/simulations/.

Brought to you by University of Alabama in Huntsville | Unauthenticated | Downloaded 02/05/25 05:57 PM UTC

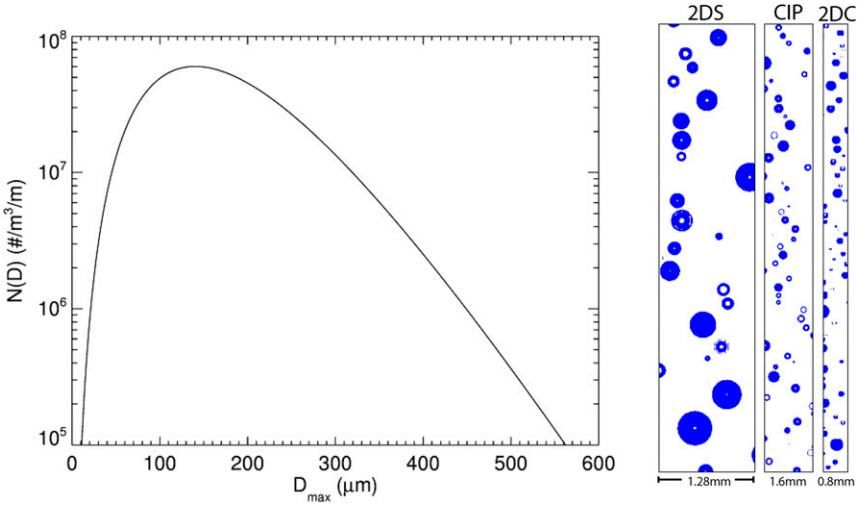

FIG. 11-5. Synthetically generated gamma function describing $N(D_{max})$ for synthetically generated particles from the 2DC, CIP, and 2DS following the procedure discussed in the text. (right) Example images from the 2DS, CIP, and 2DC for time frames of approximately 0.2, 0.25, and 0.75 s long, respectively, with scales indicated at the bottom of the figure.

functional form for the electronic response given by Baumgardner and Korolev (1997), who characterized the response for a 260X instrument with a 400-ns time constant. Strapp et al. (2001) reported response characteristics of a PMS 2DC using a spinning wire apparatus, and showed that the time constants for individual diodes on the same array can vary widely, ranging from 400 to 700 ns on the leading edge of a particle and from 300 to 900 ns on its trailing edge. The model can accommodate different response times for individual diodes but not different trailing edge time constants. The photodiode arrays used in modern instruments have much faster response times. Lawson et al. (2006) measured the response time of a 2DS at 41 ns, and Hayman et al. (2016) measured the response of the NCAR Fast-2DC (using a DMT CIP array board) at 50 ns. The effect of the electronic response time simulation for these instruments is quite small. However, other sources of delay in the full electronic system may have different response characteristics, can arise from a variety of sources, and cause substantial effects on the measured particle shape and counting efficiency (Hayman et al. 2016). These are particularly important for small particles and will likely vary between different OAP versions. Therefore, we consider the simplified electronic model used here as a best-case scenario, which can be updated as more detailed laboratory results become available.

3) Thresholding and discretization: OAPs nominally register a pixel as ''shaded'' if the illuminated light drops to 50% of the unobstructed intensity. The actual threshold may vary from diode to diode (Strapp et al. 2001), and this behavior can be simulated in the model. The diffraction and response time steps described above are performed at a resolution of 1 μm, and then the particle is resampled to the probe resolution. The simulated diodes are rectangular in shape with a 20% gap between neighboring diodes (Korolev 2007).

Data generated by this model were designed to simulate a number of instruments, including the 2DC, 2DS, CIP, CIP-Gray, 2DP, and HVPS-3. A sample of modeled images from a gamma distribution $N(D) = N_0 D^{\mu} e^{\Lambda D}$, with very few particles smaller than 100 μm in maximum dimension ($\Lambda = 28\,161.0\,\mathrm{m}^{-1}$, $N_0 = 5.18 \times 10^{24}\,\mathrm{m}^{-4-\mu}$, μ=3.95), is shown in Fig. 11-5.

In the following sections, the effect of assumptions made when processing imaging probe data is illustrated by applying varying algorithms to synthetically generated data and data measured during field campaigns. Differences are first discussed in the context of estimating the size and morphological properties of individual particles for both OAPs and other classes of imaging probes. Thereafter, uncertainties associated with estimating $N(D_{max})$ for populations of particles, eliminating spurious particles, or correcting their sizes because of partially imaged, shattered, out-of-focus particles or diffraction fringes, and with deriving bulk properties are discussed for OAPs.

b. Morphological properties of individual crystals

Algorithms for deriving morphological characteristics of individual crystals apply not only to OAPs but also to

Brought to you by University of Alabama in Huntsville | Unauthenticated | Downloaded 02/05/25 05:57 PM UTC

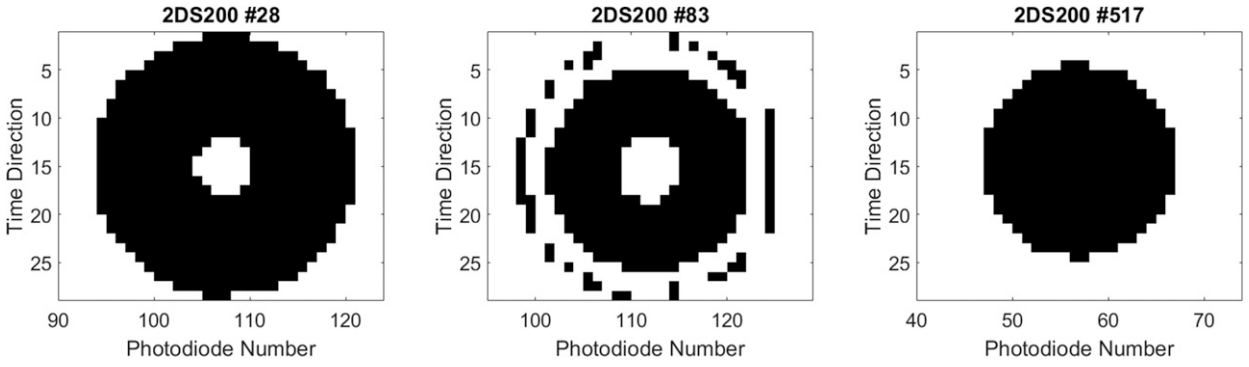

FIG. 11-6. Images of three 200-μm particles synthetically generated for a 2DS probe. Table 11-2 gives estimated L_p, W_p, D_{max}, P_p, and A_p from different processing algorithms for these 3 particles. The Z positions (relative to midpoint between the arms) of the particles are 21.4 mm (particle 28), 24.2 mm (particle 83), and 0.1 mm (particle 517).

higher-resolution optical imagers. Typically analyzed morphological properties of individual particles include the maximum dimension D_{max}, projected area A_p, perimeter P_p, and particle habit. Different algorithms used to size particles are discussed by Korolev et al. (1998b), Strapp et al. (2001), Lawson (2011), Brenguier et al. (2013), and Wu and McFarquhar (2016) for monochromatic OAPs; by Joe and List (1987) and Reuter and Bakan (1998) for grayscale probes; and by Lawson et al. (2001), Nousiainen and McFarquhar (2004), Baker and Lawson (2006), and Um et al. (2015) for higher-resolution imaging probes. In this subsection, the derivation of a metric for particle size is first discussed. Then, the use of a metric for particle morphology to derive particle habit, as applicable to any category of particle imager, is presented.

OAPs measure particles in two perpendicular directions: the first aligned with the photodiode array (width W_p) and the second along the direction of aircraft motion (length L_p). This provides a two-dimensional projection of a particle since the probe records the on/off state of the diode array at each time interval that it travels a distance of the size resolution. Alternate particle metrics, such as the maximum dimension in any direction (D_{max}) and area-equivalent diameter (D_{area}), can also be derived.

There are several uncertainties associated with deriving particle size from OAP measurements. First, when calculating L_p for legacy probes (i.e., those originally manufactured by PMS) some algorithms add an additional slice to account for the one that is missed waiting for the next clock cycle. The newer probes do not skip the first slice, hence this correction is unnecessary. Second, the meaning of L_p and W_p can be ambiguous in the case of nonspherical particles, especially with gaps or holes (unshadowed diodes within the image). These gaps or holes commonly occur when a particle is imaged by an OAP far from the object plane and is out of focus. The imaged particle gradually gets larger as it moves farther from the object plane, and a blank space can appear in its center as a result of the diffraction effect (Poisson spot; see Fig. 6 in Korolev 2007). For out-of-focus droplets, Korolev (2007) shows how the imaged size and Poisson spot diameter change with distance from the object plane, and describes the effect of digitization. Figure 11-6 illustrates examples of two synthetically generated 200-μm out-of-focus particles and one in-focus particle as would be imaged by the 2DS, with estimates of L_p, W_p, D_{max}, P_p, and A_p obtained by different algorithms shown in Table 11-2.

Even before any corrections for out-of-focus particles are applied there can be differences in how the size is derived. For example, some algorithms calculate L_p and W_p of the whole particle image, whereas others compute them for the largest continuous part of the particle. Differences for L_p, W_p, D_{max}, P_p, and A_p estimated by the University of Illinois/Oklahoma Optical Array Probe Processing Software (UIOOPS) and the University of Manchester Optical Array Shadow Imaging Software (OASIS) are 20% on average in Table 11-2 for the second particle in Fig. 11-6, but only 1.5% for the first particle. The Rosenberg software has a range of sizes as one of its inputs is the maximum distance between two shadowed pixel centers for them to be counted as part of the same particle—the range represents setting this to either 1 or 128 pixels. The first particle represents the type of out-of-focus image that is more commonly seen in OAP measurements. Given this fact, it is not surprising that there was no significant difference between estimates of L_p and W_p by UIOOPS and OASIS for 97.4% and 94.7% of all simulated 2DS particles. In-focus particles and varying degrees of out-of-focus particles are included in the sample. There are only differences in L_p and W_p when the particles

Brought to you by University of Alabama in Huntsville | Unauthenticated | Downloaded 02/05/25 05:57 PM UTC

TABLE 11-2. Morphological parameters (L_p, W_p, D_{max}, P_p, and A_p) describing three 200-μm particles synthetically generated for a 2DS probe as computed by UIOOPS, OASIS, and Rosenberg. Particle 1 refers to left particle in Fig. 11-6, particle 2 refers to the middle particle in Fig. 11-6, and particle 3refers to the right particle in Fig. 11-6. The definitions for all parameters in the table are included in the text and appendix A.

Algorithm	L_p (μm)	W_p (μm)	D_{max} (μm)	P_p (μm)	A_p (μm^2)
UIOOPS 1	280	270	280	940	5.6×10^4
OASIS 1	280	270	287	896	5.6×10^4
Rosenberg 1	280	270	283	—	5.6×10^4
UIOOPS 2	280	270	280	1380	3.8×10^4
OASIS 2	210	210	228	690	3.2×10^4
Rosenberg 2	210–280	210–270	224–287	—	$(3.2–3.8) \times 10^4$
UIOOPS 3	210	200	210	540	3.2×10^4
OASIS 3	210	200	215	652	3.2×10^4
Rosenberg 3	210	200	211	—	3.2×10^4

have gaps across their maximum length or width. The UIOOPS and OASIS give different values for this particle's D_{max}. The Rosenberg software can be set up to match either of the other two methods. In general, the Rosenberg software sets D_{max} to be the distance between the two most distant pixels plus 1 pixel, and UIOOPS sets D_{max} according to the diameter of the largest circle encompassing the particle. Differences between P_p for OASIS and UIOOPS are due to using only contiguous or all shadowed pixels. Rosenberg does not provide P_p as it uses other methods for habit identification. Based on these comparisons of raw image properties, the biggest uncertainty in estimating the true sizes of out-of-focus particles is the application of adjustments to the sizing of out-of-focus particles.

Most algorithms use a lookup table following Korolev (2007) for correcting the sizes of out-of-focus spherical particles. This algorithm uses the Fresnel diffraction approximation to deduce particle size and its distance from the object plane from the morphological properties of the image and the size of the Poisson spots. No algorithm is available to correct the sizing of nonspherical out-of-focus particles. Some studies have applied the correction algorithm to ice crystals, particularly in mixed-phase and ice clouds, using the justification that the crystals were quasi-spherical. This application, however, can possibly introduce additional uncertainty since oftentimes thin, platelike crystals will be semitransparent and their images will appear with unocculted diodes in their center. Hence, until a better methodology is developed to identify and correct out-of-focus crystals, application of a Korolev-type correction is not recommended.

Further difficulties and increased uncertainties occur when trying to size partial images, namely, those where the shaded areas touch or overlap the edge of the image boundaries. Treatment of such images is inconsistent between software, and for OAPs many algorithms have corrections for sizing such particles. Some software apply the Heymsfield and Parrish (1979) method, which calculates D_{max} assuming a spherical shape for all imaged particles whereas others use only particles whose center is inside the photodiode array (i.e., maximum dimension in time direction does not touch array edges) or use only particles entirely within the array, or apply no adjustments whatsoever. Korolev and Sussman (2000) summarize the Heymsfield and Parrish (1979) approach for treatment of partial images.

Estimates of A_p for partially imaged particles can also be different: for particles entirely in the diode array, A_p is the number of diodes shadowed multiplied by diode resolution squared. But partially imaged particles might have A_p estimated from published relations (e.g., Mitchell 1996; Heymsfield et al. 2002b; Schmitt and Heymsfield 2010; Fontaine et al. 2014) between A_p and particle dimension or through reconstruction. Other differences may occur in how particle size is adjusted to correct for under or oversampling, which occurs if the slice rate is incorrectly set because of an incorrect airspeed controlling the sampling.

Although grayscale OAPs provide additional information about the level of shading of photodiodes, derived particle size is different depending on whether a 25% (for 2D-G; CIP-G uses 30% instead), 50% or 70% change in illumination is used by the software: clearly more pixels will be shadowed at 50% than at 70% resulting in a larger derived size. Figure 11-7, constructed from airborne measurements of liquid water droplets with a 25-μm CIP-G, shows that using a 70% shadowing level results in derived diameters approximately 100 μm lower than when a 50% shadowing level is used, with even larger differences for the smallest particles. The 50% shadowed images that are out of focus have been corrected using the Korolev (2007) methodology. A similar methodology has not been developed for imaging at 70%, so no correction is applied to the length derived from the 70% level shown in Fig. 11-7.

Brought to you by University of Alabama in Huntsville | Unauthenticated | Downloaded 02/05/25 05:57 PM UTC

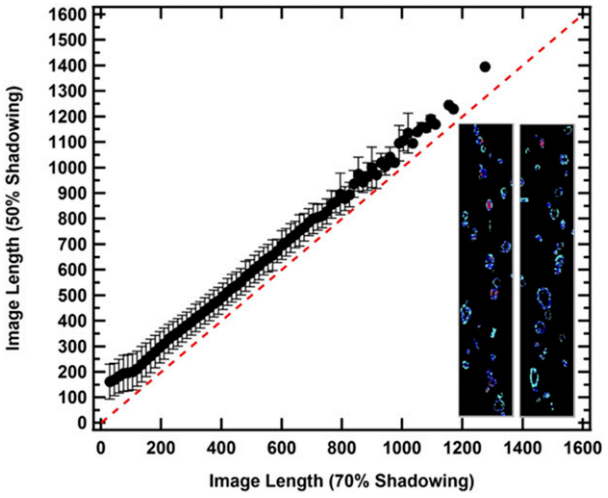

FIG. 11-7. Relationship between particle length determined from a gray probe depending upon whether 70% or 50% shadowing was used to define the particles. This comparison was constructed from water droplets measured with an airborne CIP-Gray probe. The embedded filmstrip shows representative particles that were imaged by the probe for the time period analyzed.

There are several different ways in which $D_{\max}$ can be defined (Battaglia et al. 2010; Lawson 2011; Brenguier et al. 2013; Wood et al. 2013) for cloud particle images. Wu and McFarquhar (2016) evaluated six commonly used definitions of $D_{\max}$ for ice clouds: 1) maximum dimension in the time direction L_p; 2) maximum dimension in the photodiode array direction W_p; 3) the larger of L_p and W_p (D_L); 4) the mean of L_p and W_p (D_A); 5) the hypotenuse of a right-angled triangle constructed from L_p and W_p (D_H); and 6) the diameter of the smallest circle enclosing particle D_S. The evaluation focused on how the application of these six definitions affected $N(D_{\max})$ for OAPs. As shown in Fig. 11-8, $N(D_{\max})$ can differ by up to a factor of 6. It should be noted that for liquid or nearly spherical particles each of these definitions should yield a similar value. However, for other particles significant differences are expected and it is not always clear which definition is closest to $D_{\max}$ because a two-dimensional shadow of a three-dimensional particle with arbitrary orientation with respect to the optical plane is seen. Ice particles with $D > 100\,\mu$m have preferential orientation while falling in air (Pruppacher and Klett 1997) so that particles imaged by probes with a vertical orientation of the laser beam have silhouettes with close to the maximum particle projection. Following Um and McFarquhar (2007), an iterative procedure for pristine, regular particle shapes can be followed to estimate the three-dimensional size, but this still does not represent a direct measure in three dimensions.

Varying measures of particle morphology (L_p, W_p, $D_{\max}$, A_p, P_p, etc.) are also used to identify particle habits using a number of classification schemes. In addition to manual classification, such schemes have used morphological measures of crystals (e.g., Holroyd 1987; Um and McFarquhar 2009, hereinafter UM09), neural networks (McFarquhar et al. 1999), pattern recognition techniques (Duroure 1982; Moss and Johnson 1994), dimensionless ratios of geometrical measures (Korolev and Sussman 2000), principal component analysis (Lindqvist et al. 2012), characteristic positions of triggered pixels (Fouilloux et al. 1997), and Fourier analysis (Hunter et al. 1984) to assign shapes. These habit classification schemes have been developed and implemented for OAPs and other cloud imagers.

Uncertainties associated with such schemes are illustrated using data collected by a cloud particle imager (CPI) during the Tropical Warm Pool International Cloud Experiment (May et al. 2008) and the Indirect and Semi-Direct Aerosol Campaign (McFarquhar et al. 2011b). Data from the CPI are used because it has higher-resolution than the OAPs and hence allows an assessment of how the methodology itself, rather than the limited resolution of images, affects the identification of shape. Figure 11-9 shows inferred habit distributions based on the UM09 algorithm and the SPEC CPIView software (SPEC 2012). Large differences in habit definition evident in this figure are caused by a number of factors. First, there is ambiguity in the definition of habit categories. Although several categories are common (i.e., column, plate, and bullet rosette), other categories differ (e.g., bullet rosettes, aggregates, and irregulars). The number of categories also differs, with manual classifications (e.g., Magono and Lee 1966; Katsuhiro et al. 2013) typically having more categories than shown in Fig. 11-9. In general, the fraction of pristine crystals (i.e., column and bullet rosettes) identified by different methods are comparable, while those for nonpristine or irregular crystals, which frequently dominate habits (e.g., Korolev et al. 1999; Um et al. 2015), are not. Morphological measures of particles (e.g., L_p, W_p, $D_{\max}$, A_p, and P_p) can differ depending on the threshold values used to extract them (Korolev and Isaac 2003).

Similar schemes can be applied to OAPs, with their applicability depending somewhat on the resolution of the sensor. In some studies, such as Jackson et al. (2012), habit-dependent size distributions are generated by applying the fraction of size-dependent, identified habits (by the CPI) to size distributions measured by OAPs. This approach takes advantage of the higher resolution of the CPI complemented by the larger and more well-defined sample volume of the OAP.

Brought to you by University of Alabama in Huntsville | Unauthenticated | Downloaded 02/05/25 05:57 PM UTC

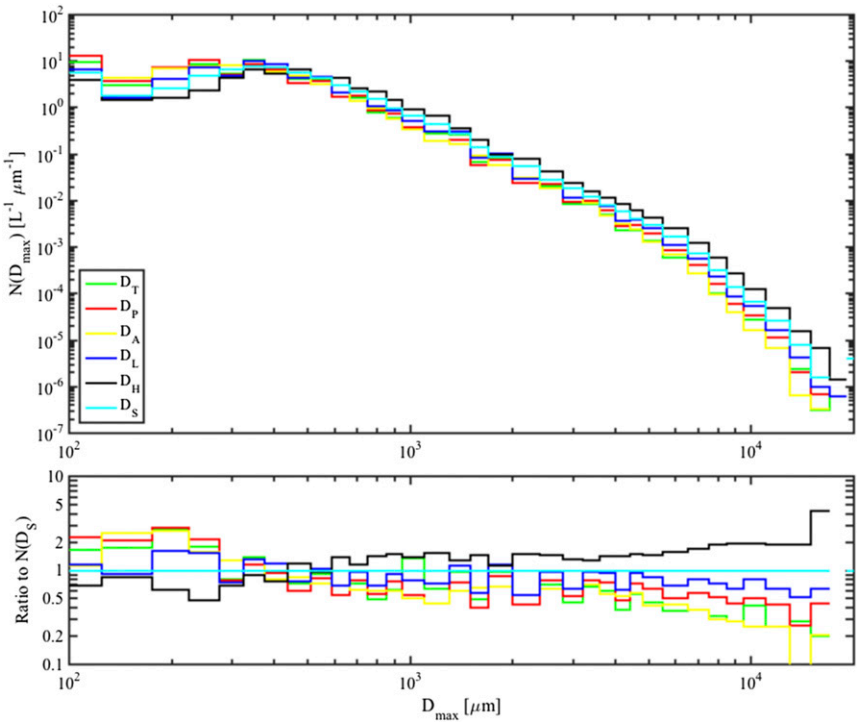

FIG. 11-8. (top) $N(D_{\max})$ as function of $D_{\max}$ using six different definitions of $D_{\max}$; (bottom) the ratio of $N(D_{\max})/N(D_s)$ for $D_{\max}$ using different definitions of maximum dimension indicated by D_T, D_P, D_A, D_L, D_H, and D_s for data collected in the trailing stratiform region of a mesoscale convective system sampled on 20 May 2011 during the Mid-Latitude Clouds, Convection and Chemistry Experiment (MC3E). Adapted from Wu and McFarquhar (2016), who provide the definitions of D_T, D_P, D_A, D_L, D_H, and D_S. The D_T and D_P are denoted as L_p and W_p, respectively, in this study.

c. *Computation of* $N(D_{\max})$

Figure 11-10 illustrates the variability between several processing algorithms when generating $N(D_{\max})$ from the same raw data file obtained by a CIP and PIP installed on the NOAA P-3 aircraft during Hurricane Isaac (2012). This comparison may exaggerate the expected difference in $N(D_{\max})$ between algorithms because of varying degrees of quality control that were applied. Nevertheless, it is seen that the degree of uncertainty in $N(D_{\max})$, induced by the processing, approaches two orders of magnitude.

Sample volume per unit time (SV) is required to determine $N(D_{\max})$ or concentration from a set of images taken over a specific duration. The method for determining SV is relatively standard across OAPs, but can vary for other imaging probes. For OAPS it is given by

$$\mathrm{SV} = \mathrm{TAS} \times \mathrm{SA} = \mathrm{TAS} \times \mathrm{EAW} \times \min(\mathrm{Sep}, \mathrm{DOF}), \tag{11-7}$$

where TAS is the true airspeed perpendicular to the optical array and the laser path, SA is the sample area, EAW is the effective array width, which is a function of the optical array geometry W_p and the method for dealing with particle shadows, Sep is the separation of the instrument arms, and DOF is the instrument depth of field.

Three analysis methods are considered for determining EAW. In the ''entire in'' case, a shadow must not include either the first or the last diode otherwise it is rejected. In the ''center in'' method, the center of a circular shadow must be imaged, but it is permitted for edge diodes to be shadowed. For both these options EAW can be determined by simple geometric arguments. A third method is a reconstruction technique described by Heymsfield and Parrish (1979; HP79 below). The three methods give the following estimates for EAW:

$$\mathrm{EAW} = \begin{cases} Nw, & \text{center in} \\ Nw + 0.72D_{\max}, & \text{HP79} \\ (N-1)w - W_p, & \text{entire in} \end{cases}, \tag{11-8}$$

where N is the number of photodiodes and w is the width or resolution of an individual photodiode.

Brought to you by University of Alabama in Huntsville | Unauthenticated | Downloaded 02/05/25 05:57 PM UTC

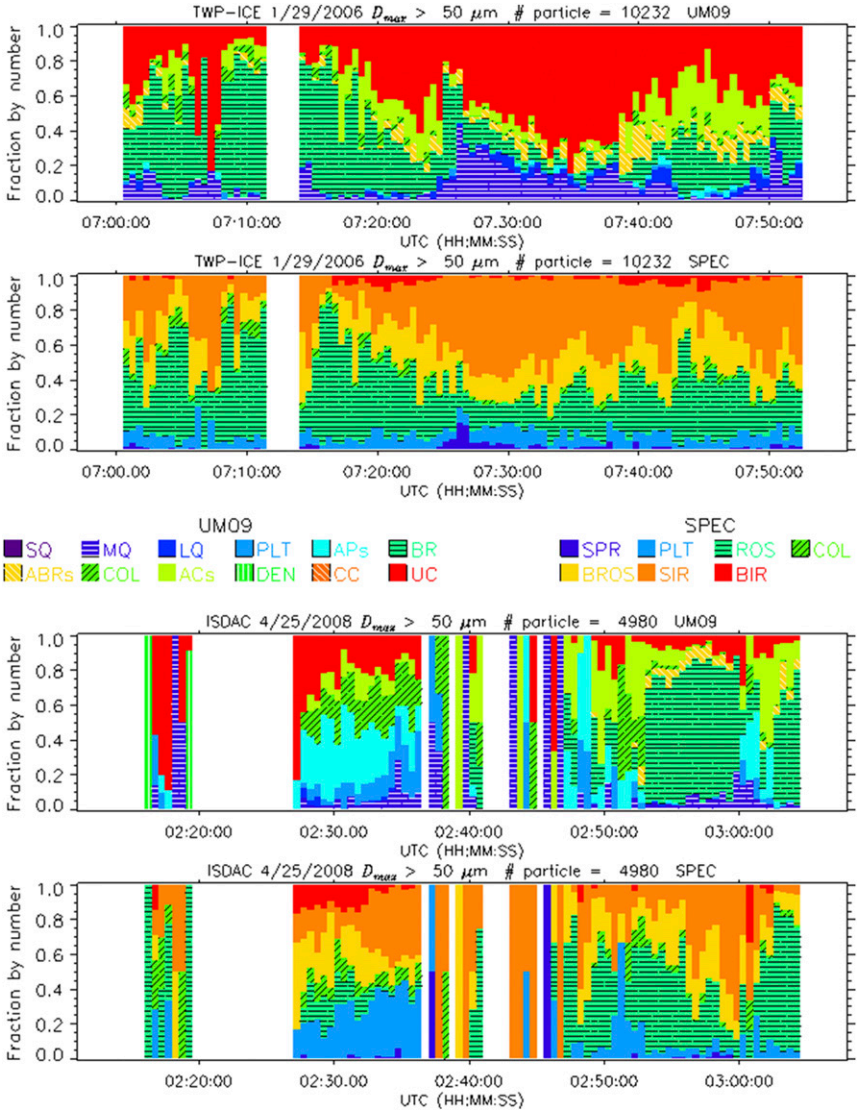

FIG. 11-9. Habit fraction by number for 30-s time intervals produced from different algorithms [UM09 and SPEC CPIView (SPEC)] for ice crystals with $D_{\max} > 50\,\mu$m imaged by CPI during the (top) Tropical Warm Pool International Cloud Experiment (TWP-ICE) and (bottom) Indirect and Semi-Direct Aerosol Campaign (ISDAC). UM09 has 12 habits: small- (SQ), medium- (MQ), and large-quasi sphere (LQ), plate (PLT), aggregates of plates (APs), bullet rosette (BR), aggregates of bullet rosettes (ABRs), column (COL), aggregates of columns (ACs), dendrite (DEN), capped column (CC), and unclassified (UC). SPEC has 7 habits: spheroid (SPR), PLT, rosette (ROS), COL, budding rosette (BROS), small irregular (SIR), and big irregular (BIR).

The DOF is defined by the diffraction of the light by the measured particle. Particles farther from the optical plane cause less deep shadows until eventually they do not shadow any photodiodes above the required amount for detection. The distance between points on either side of the optical plane where particles disappear defines the DOF, which is double the distance a particle can be from the object plane and still shadow a photodiode by the appropriate preset threshold. As was shown experimentally by Knollenberg (1970) and then analytically by Korolev et al. (1998b) the diffraction pattern of a spherical particle is a function of the dimensionless parameter $Z_d = \lambda_l |Z|/R^2$, with Z the distance between the particle and object plane, λ_l the laser wavelength and R the particle radius, which would be $D_{\max}/2$ for spherical particles. The implications for nonspherical particles are discussed below.

Thus, the DOF is typically represented as $2gR^2/\lambda_l$ with the DOF's maximum value set by the distance between

Brought to you by University of Alabama in Huntsville | Unauthenticated | Downloaded 02/05/25 05:57 PM UTC

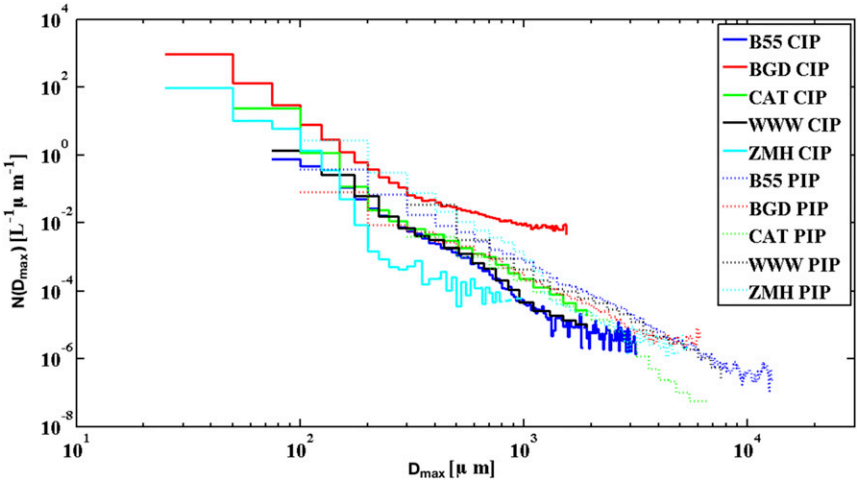

FIG. 11-10. $N(D_{max})$ as a function of D_{max} from several processing algorithms applied to the same raw data file obtained by a CIP and PIP installed on the NOAA P-3 aircraft in Hurricane Isaac in 2012. The three-letter acronyms in front of the CIP/PIP refer to different processing algorithms: the specific algorithms for each SD were not identified at the 2014 MIT workshop.

probe arms. Knollenberg (1970) used $g = 3$ for a shadow threshold of 50%. For the same shadow threshold, Lawson et al. (2006) found from laboratory calibrations that $g = 8$ for the 2DS, which is consistent with the theoretical value of DOF for the 50% threshold intensity level of $g = 8.18$ found by Korolev et al. (1998b). It should be noted that DOF is sensitive to the settings of the photodiode's intensity threshold, and it may vary from probe to probe (Korolev et al. 1998b; Strapp et al. 2001). In this regard, g should ideally be separately determined for each individual probe, with particles not entirely within the field of view and the nonspherical nature of ice crystals complicating the choice. The DOF is especially uncertain for particles with $D_{max} < \sim 150\,\mu$m (Heymsfield and Baumgardner 1985; Baumgardner and Korolev 1997). This is because DOF is dependent upon size squared and size is uncertain for small particles when the shadow is only a small number of pixels across; for $D_{max} > \sim 150\,\mu$m the DOF is similar to the arm separation and the sample volume is hence less uncertain. Given that the DOF is small for such sizes, only a few counts in channels corresponding to these sizes can produce large and highly uncertain calculated concentrations. Generally, 100 particles in a size bin is regarded as statistically significant (Hallett 2003).

The DOF is also sensitive to the TAS if the electronic response of the photodiodes decreases with increasing airspeed (Baumgardner and Korolev 1997). The obscuration intensity decreases with the particle distance from the center of focus. For sensors whose diode response decreases with airspeed, although the actual shadow on the array may be 50% of the value at the center of focus, the measured occultation may be only some fraction of that. Hence, to be measured at 50%, the particle would have to pass closer to the center of focus to cast a shadow darker than 50%. This means that the g value would be TAS dependent (Baumgardner and Korolev 1997).

Although spherical particles with fixed R have been used in laboratory studies to derive the value of g, ice crystals are typically nonspherical in nature. Thus, there is some ambiguity in the choice of particle dimension that should be used to represent R in the DOF calculation for the data processing algorithms. Some studies use $R = D_{max}/2$, whereas others use $L_p/2$ or $W_p/2$. There is no consensus on the definition of R that should be used for calculating the DOF (Brenguier et al. 2013). The derivation of SDs in terms of D_{max} is preferable given that D_{max} serves as the basis of many parameterization schemes developed with data. Perhaps a definition of DOF in terms of W_p, but representation of SDs in terms of D_{max} may be optimal, but thus far no processing algorithm has implemented such an approach.

The clocking rate of the OAP affects both the sizing of the particle and calculated SDs through its impact on the SV. Because the OAP geometry or the aircraft itself represents an airflow distortion, TAS at the location of the OAP SV may not equal the speed of the aircraft body through the air (Krämer et al. 2013). Early studies found that cloud physics probes mounted on the aircraft fuselage can be affected by large distortions in airflow and particle trajectories at the probe location caused by flow around the fuselage (King 1984, 1985; King et al. 1984; Norment 1985; Twohy and Rogers 1993). This is

Brought to you by University of Alabama in Huntsville | Unauthenticated | Downloaded 02/05/25 05:57 PM UTC

further discussed in chapter 9 (Baumgardner et al. 2017) in section 6 under the subheading ''Impact of mounting location.'' Most OAP probes are now mounted in select locations below the aircraft wing, where distortions due to the aircraft itself are usually smaller. However, local distortions in TAS and flow angle are still possible because of varying airflow about the wing, through the OAP arms, or compression upstream of the housing itself (Norment 1988; Weigel et al. 2016). A bias in a local static reference point due to slowing airflow can have a large impact on the calculated TAS. Computational fluid dynamics studies and empirical corrections are useful for handling these effects (Weigel et al. 2016). In addition, a simple method of adjusting image aspect ratios to expected values can be used if preferentially oriented crystals are not present (King 1984, 1985; King et al. 1984).

For legacy probes, particle images are typically stored in two buffers so that one can be used to store images when data from the other are transmitted to the data system. But, in clouds with high concentrations, the second buffer can fill up while the first is still transmitting. In this case, there will be a dead period when no data are recorded. For some newer probes (e.g., the 2DS), the probes skip individual particles in overload and keep track of the dead time so that the sample volume can be corrected. Other probes, such as the CIP and PIP, have a counter that keeps track of skipped particles so that SDs can be reconstructed. However, when the CIP buffers are full, only the number of particles and W_p are recorded without timing information. This means that during overload periods it is difficult to make corrections for shattered particles (see below). In any event, checks should ensure that the sum of particle interarrival times matches the record time to insure the timing information is correctly recorded. Implementation of such corrections in different algorithms may cause discrepancies in the derived $N(D_{\max})$.

d. *Removal of spurious particles*

Additional algorithms are applied to remove artifacts from the measured data. As discussed in chapter 9 (Baumgardner et al. 2017), small crystals can be generated from the shattering of larger crystals on the protruding tips and inlets of probes. These do not represent naturally occurring crystals. There are algorithms that attempt to eliminate shattering artifact particles based on the time between particle arrivals in the sample volume (Cooper 1978; Field et al. 2003, 2006) (i.e., interarrival time τ_i), and on the numbers, sizes, and gaps between fragments in a single image (Korolev and Isaac 2005). Further elaboration and analysis of limitations of

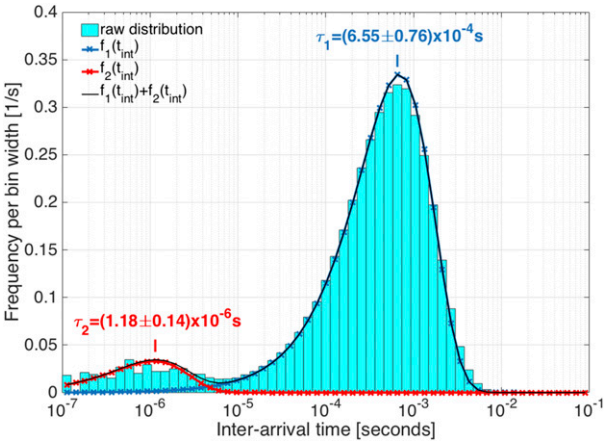

FIG. 11-11. Normalized frequency distribution of interarrival times recorded by a 2DS probe installed on a French Falcon aircraft during the collaborative 2014 HAIC/HIWC project on 18 Feb 2014. Solid lines represent best fits to modes of peaks describing naturally occurring particles and shattered artifacts, generated following approach of Jackson et al. (2014).

the interarrival time algorithm was described in Korolev and Field (2015). Many studies have implemented such algorithms (e.g., Baker et al. 2009; Korolev et al. 2011, 2013c; Lawson 2011; Jackson et al. 2014).

The basis of interarrival time algorithms (e.g., Field et al. 2006; Baker et al. 2009; Lawson 2011; Korolev et al. 2011, 2013b; Jackson et al. 2014) is that a bimodal Poisson probability density function describes the distribution of τ_i, where particles occurring in a peak with a larger mode τ_1 correspond to naturally occurring particles and those in a peak with a smaller mode τ_2 correspond to potentially shattered particles. Figure 11-11 shows a distribution of interarrival times measured by a 2DS probe installed on the French Falcon aircraft during the collaborative 2014 European High Altitude Ice Crystals and the North American High Ice Water Content projects (HAIC/HIWC); similar figures showing distributions of interarrival times or distances are found in Lawson (2011), Korolev et al. (2011, 2013b), Jackson et al. (2014) and others. The peak at an interarrival time of 6×10^{-4} s corresponds to naturally occurring particles, whereas the peak at an interarrival time less than 10^{-6} s corresponds to shattered artifacts. Generally there may be some overlap between the two modes and different approaches exist for choosing a threshold τ_i so that few naturally occurring particles are removed and most artifacts are removed.

Examples of different approaches for making interarrival time corrections are illustrated in Fig. 11-12, which shows the frequency distribution of interarrival times recorded by the 2DS during HAIC/HIWC as a function of time. The different colored lines show how

Brought to you by University of Alabama in Huntsville | Unauthenticated | Downloaded 02/05/25 05:57 PM UTC

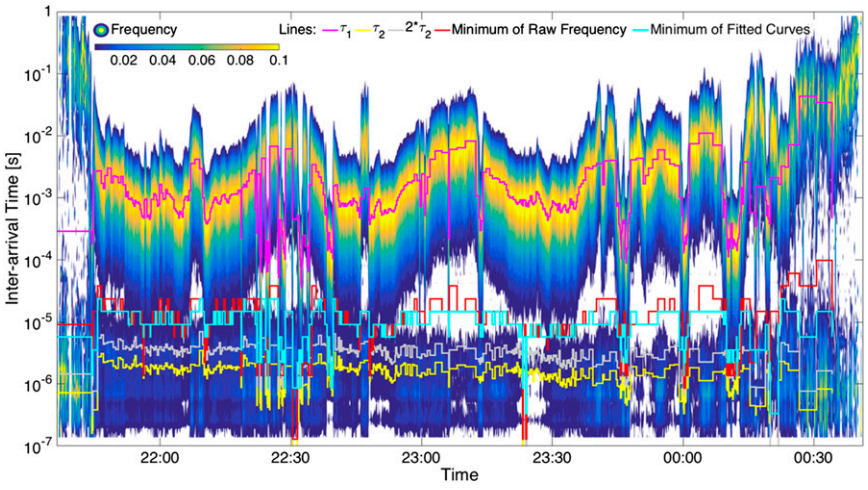

FIG. 11-12. Normalized frequency distribution of interarrival time as function of flight time for HAIC/HIWC flight on 18 Feb. 2014. Different colored lines represent τ_1 (purple), τ_2 (yellow) and three different thresholds used to define boundary between naturally occurring particles and shattered artifacts: twice τ_2 (gray), the interarrival time between τ_1 and τ_2 with smallest measured frequency of occurrence (red, minimum of raw frequency) and the interarrival time between τ_1 and τ_2 with the smallest frequency of occurrence based on fit curves to the frequency of occurrence for the two Gaussian distributions (cyan, minimum of fitted curves).

τ_1, τ_2, and thresholds used to define the boundary between naturally occurring particles and shattered artifacts vary with time. The different methodologies used to define this threshold include the following: $2 \times \tau_2$ (gray), the interarrival time between τ_1 and τ_2 with smallest measured frequency of occurrence (red, minimum of raw frequency), and the interarrival time between τ_1 and τ_2 with the smallest frequency of occurrence based on fit curves to the frequency of occurrence for the two Gaussian distributions (cyan, minimum of fitted curves). There can be large differences in the interarrival time threshold between methods and in their temporal variation. Some algorithms define a single threshold representative of the whole flight, others use a specific number of sequentially observed particles (e.g., 2000), a fixed time frame (e.g., 5 min), or a flexible time frame for defining the temporal variation. Flexible time frames can be dependent upon the overall concentration for each time or the computed mean particle spacing (Lawson 2011). In addition, when an artifact is identified through interarrival time analysis, that particle and one or two adjacent particles are removed (depending on the selected algorithm). The impact of such differences has not been well documented over a range of conditions, but can have a big impact on calculated $N(D_{\max})$. Other algorithms (e.g., Lawson 2011) use the interarrival distance (TAS divided by interarrival time) rather than the interarrival time so that the threshold is not sensitive to TAS. Often, shattered particles can be found as a stream of consecutive particles with independent time stamps or, if close enough in space, they can be recorded as a single image of widely spaced, unconnected pixels. In the former case the stream of shattered particles will be removed by an interarrival time or distance algorithm. In the latter case, other image-filtering methodologies (described below) will likely eliminate them.

There is also the possibility that some particles rejected on the basis of interarrival times should be accepted. There are two reasons for this: 1) if the natural crystals are located uniformly random in space, some fraction of them will be separated by a distance shorter than the distance selected as the shattering threshold, and 2) it is possible for diffraction fringes around large particles to confuse interarrival time algorithms as these could be identified as multiple particles on a single image. To counter the latter problem, some algorithms (but not all) reaccept these particles when their size is above a selected threshold since most shattered particles are smaller than 500 μm (Korolev et al. 2013b,c).

Shattered or other anomalous particles (e.g., caused by stuck diodes or streaks of water across the probe in mixed-phase clouds) can also be rejected based on particle shape or on the numbers, sizes, and gaps between fragments in an image frame. Algorithms can also remove fragment images that appear as a result of diffraction effects (e.g., Fig. 3 in Korolev and Field 2015). To deal with such artifacts, the area ratio is defined as A_p divided by the area of a circumscribed circle with diameter $D_{\max}$ (McFarquhar and Heymsfield

Brought to you by University of Alabama in Huntsville | Unauthenticated | Downloaded 02/05/25 05:57 PM UTC

1996). Particles with area ratios less than 0.1 or 0.2 are commonly identified as artifacts. It is worth noting that there is little consistency between algorithms in how/if shatter artifacts, diffraction fringe artifacts, and other image artifacts are dealt with. These differences contribute to variations in the subsequently derived $N(D_{\max})$.

e. Derivation of bulk properties

Based on the derived $N(D_{\max})$, a number of bulk cloud microphysical properties related to various moments of the distribution can be derived where

$$M_n = \int_{D_0}^{D_1} N(D_{\max}) D_{\max}^n \, dD_{\max}, \qquad (11\text{-}9)$$

where M_n is the nth moment of the distribution, and D_0 and D_1 are the minimum and maximum diameters over which $N(D_{\max})$ was measured. Thus, the total number concentration is M_0 and $w_i = aM_b$ when the mass of an individual ice particle is represented as $aD_{\max}^b$, where a and b are habit-dependent coefficients (Locatelli and Hobbs 1974; Mitchell 1996). Higher-order moments can also be represented in terms of other measures of particle morphology, such as Baker and Lawson's (2006) calculation of particle mass in terms of projected area. Uncertainties in derived bulk properties are dependent upon uncertainties in $N(D_{\max})$ and the applicability of the relevant algorithm used to define properties of individual particles. For example, Field et al. (2006) and Jackson and McFarquhar (2014) found small crystal artifacts produced by shattering make estimates in total concentration highly uncertain because the zeroth-order moment is highly dependent on concentrations of particles with $D_{\max} < 500\,\mu$m, namely, those particles produced by shattering. But, estimates of w_i had at most 20% uncertainty from shattering because its higher-order moment is more dominated by larger particles not generated by shattering; in fact, uncertainties associated with estimating a three-dimensional shape and density from a two-dimensional image are larger.

Derived bulk properties are sensitive to the definition of $D_{\max}$ (Wu and McFarquhar 2016). For instance, D_m can vary by 2 times, w_i as much as 3 times, and β up to 2 times, depending on the definition used.

f. Processing, analysis, and presentation software

A number of different software packages are used for processing, analyzing, and presenting data from cloud probes. In this section, a path forward is discussed for creating community-based open-source software that will make differences in processing algorithms more transparent. Since the most complex processing algorithms are for data collected by OAPs, this section concentrates on code that processes these types of spectrometers.

Available processing codes for OAPs include the System for OAP Data Analysis (SODA) developed at NCAR; OASIS; UIOOPS; the Airborne Data Processing and Analysis (ADPAA) developed at the University of North Dakota, the Software for Airborne Measurements of Aerosols and Clouds (SAMAC; Gagne et al. 2016); and software packages developed at SPEC Inc., Environment and Climate Change Canada, and Leeds University (Rosenberg software referenced previously). Although there are differences between codes with respect to the programming language, platforms supported, and algorithms by which data are processed, there are also many common features: all algorithms convert raw measurements into single-particle data that are used to derive SDs and bulk cloud properties.

Because there are many different codes for processing data from OAPs and the inherent algorithms and codes may change occasionally, a detailed discussion of the individual algorithms is not provided here. However, it is noted that most codes can handle data from a variety of data acquisition systems, raw data formats, and buffering schemes. Morphological measures of the derived single-particle properties typically include various properties that could be used to define $D_{\max}$ (e.g., the diameter of the minimum enclosing circle, or maximum length in the photodiode or time array), projected area, aspect ratio (Korolev and Isaac 2003), particle habit, and a measure of the complexity of the image. Corrections are applied for out-of-focus, undersampled, or partially imaged particles and for diffraction (e.g., Korolev 2007), and particles are rejected depending on image shapes (aspect or area ratio), interarrival time or spacing distance (e.g., Field et al. 2006) or particle center located outside the photodiode array. The $N(D_{\max})$ and bulk properties are then determined using the size-dependent sample volume. Many codes also provide utilities for data display and visualization, computation of derived bulk quantities, merging probes with different size ranges, and data export. Codes may or may not include a graphical interface.

Currently, distribution of OAP processing codes is complicated because they are continually undergoing changes as new algorithms are introduced or old ones edited. In addition, as new instruments come on line, changes are needed in existing codes to accommodate them. Furthermore, changes in the codes sometimes are necessary when processing data from a different version of the same probe, or more sophisticated tuning is mandated when processing data from the same probe used in different conditions. Therefore, it is a challenge for investigators who are not code developers to grasp to grasp the sensitivity of derived

Brought to you by University of Alabama in Huntsville | Unauthenticated | Downloaded 02/05/25 05:57 PM UTC

products to the assumptions that were used to process the measurements. Hence, developers are reluctant to freely distribute their software without associated caveats. Even if a community code is developed, it will require continual updates and modifications.

Many of these issues were discussed at the 2016 EUFAR International Commission on Clouds and Precipitation (ICCP) workshop on data processing, analysis, and presentation software of cloud probes at the University of Manchester. Although consensus was not reached by the participants on the optimum procedures for processing cloud probe data, it was unanimous that the need is urgent for a common reference library, including the individual processing algorithms. For inclusion in this library, algorithms or software packages should either have been published in the refereed literature or have passed through a mutually agreed upon, peer reviewed, internal vetting process. The need for using some form of version control, the strong desire for open-source software, and the recommendation of assigning a digital object identifier (DOI) for individual processing algorithms was also emphasized. However, given the dynamic nature of the codes it may prove difficult to assign a DOI to such codes. Hence, some other approach for referencing and making codes available may be required. The availability of synthetic datasets and benchmark cases for evaluating new algorithms was also noted as another critical component for evaluating new or updated algorithms. The need for future workshops to continue these collaborations was also aknowledged.

5. Future efforts

Since the development of cloud probes more than 50 years ago, processing algorithms have been developed to derive single-particle properties, size distributions, and bulk parameters for ice clouds. Significant progress has been made in understanding the basic sensing principles and inherent measurement uncertainties that have led to correction algorithms for issues such as conduction and convection from a heated wire to the surrounding cold air. While adjustments to concentration data are well known and documented for scattering probes, the sizing of ice crystals is less certain. Artifical shattering of ice crystals is a problem for both light-scattering spectrometers and particle-imaging probes, but antishattering tips and spurious particle removal algorithms have helped correct for this issue. In addition to shattering, concentration data from particle-imaging probes can be greatly affected by numerous other issues including maximum dimension definition, depth of field calculation, effective array width choice, image diffraction, and true airspeed assumption. The details and assumptions in some of these processing algorithms can have large effects on the derived cloud products. With the application of various codes by different groups and no clear consensus on the optimal methodology for processing data, it remains a challenge to compare data processed by different groups, or sometimes even by the same group, from different field campaigns. In addition, the specific calibration for individual probes may not be known or available so that differences in calibrations can introduce additional uncertainties. Further, the exact set of assumptions used to process data from a particular field project is not always clear, and even if such assumptions were well documented, their effect on derived properties is not well known. Therefore, it is difficult to make progress on understanding how cloud properties vary with geographical location and environmental conditions, a prerequisite for understanding cloud processes and improving the representation of these processes in weather and climate models.

Processing algorithms for interpreting data from total water content and forward-scattering probes are more mature than for those for imaging probes. For heated sensors, estimating the dry-air term and removing baseline offsets are the largest uncertainties. For total water content probes that vaporize cloud droplets and ice crystals, removing the baseline offset, estimating particle cut sizes from the counterflow, and determining the importance of particles bouncing out of the sensor volume are the biggest unknowns. For forward-scattering probes, coincidence and shattering adjustments, calibration of bin boundaries to account for oscillations in instrument response, and sizing nonspherical ice crystals are the largest uncertainties. Ongoing efforts to intercompare algorithms in water clouds improve our understanding of how algorithms perform in ice because closure studies are simpler in the presence of spherical water drops.

Uncertainties in processing image probe data and discrepancies between processing codes are especially prevalent. To reduce the uncertainties associated with processing of measurements and to make assumptions used in processing data more transparent, more methodical algorithm comparisons are needed. In particular, a raw or synthetic data file (i.e., a benchmark) should be processed by several groups in sequential steps. For example, raw counts as a function of size for complete, partial and total images should be compared before comparing derived SDs. Thereafter particular image correction techniques (e.g., particle reconstruction, corrections for out-of-focus particles) and particle rejection algorithms should be sequentially activated in each code, with results compared after each step. This will identify sources of discrepancies in algorithms and show how different assumptions affect and lead to uncertainty in derived products. Furthermore,

Brought to you by University of Alabama in Huntsville | Unauthenticated | Downloaded 02/05/25 05:57 PM UTC

this should help establish best practices for processing OAP data that could be widely adopted by different groups. Other specific recommendations for OAPs include the following:

1) Evaluation of grayscale probes to see if a better definition of the DOF is possible;
2) further investigations of the nature of the DOF, including its dependence on size and determining if a definition better than $2gR^2/\lambda_l$ is possible;
3) applications of consistency checks on collected datasets, such as determining if all diodes in the array have uniform responses throughout the experiment;
4) closure tests to check that the sum of all channels in the recorded 1-Hz distributions is equal to those determined from the individual image counts.

Table 4.1 of Isaac and Schmidt (2009) lists possible accuracies of different parameters derived from in situ sensors. Chapter 9 (Baumgardner et al. 2017) of this monograph is focused on instrument limitations and measurement uncertainties and updates the Isaac and Schmidt (2009) information to give quantitative uncertainties in total water content and light-scattering and imaging probes associated with the measurement techniques themselves. In this paper, no attempt has been made to quantitatively summarize the accuracy of quantities derived from the processing algorithms. Despite significant progress in the past 10 years, the development and interpretation of processing techniques has revealed more issues that were not previously recognized or thought to be important (e.g., ice shattering, local airspeed in probes' sample areas, ice bouncing on hot wires, and particle reacceptance in processing software). This new knowledge gives a retrospective on the quality of past assessments of measurement accuracy, and some new estimates of accuracy have been increased compared to past estimates. Many of the errors are nonlinear and depend on the value of the measured parameter, and hence cannot be easily summarized in a table. One of the biggest obstacles hindering progress in understanding accuracy is the absence of measurement standards for particle concentration, ice water content, and ambiguity in sizing of nonspherical particles. Thus, presenting a summary table on instrument accuracy would be premature.

In addition, it is necessary for the community to develop a strategy toward a consensus as to which assumptions are optimal when processing in situ data from heated sensors and forward-scattering and imaging probes. A community workshop, a community survey, and code comparisons would be beneficial in making these recommendations. However, there cannot be a stagnant code or a frozen best approach for processing data: inevitably the optimum algorithms will evolve over time as more is learned about the performance of the various probes and more sophisticated algorithms are introduced and evaluated. Thus, all processing codes should be open source, version controlled, and well documented, preferentially with a DOI, even though this is difficult with dynamic codes. With this approach, both code developers and data users are equally able to process microphysical probe data. Finally, given the agreement that all algorithms should be either published or approved by a panel of experts, it may be appropriate for a governing body or organizing entity to make recommendations for best practices.

Ultimately, it would be of general benefit to develop a community software package that incorporates different algorithms and assumptions for processing the data (e.g., different algorithms for correcting out-of-focus particles or rejecting shattered artifacts for imaging probes). Examples and tutorials should be available to expand the range of code users. Similar approaches have been followed for the development of both weather and research forecasting models (e.g., Skamarock et al. 2008) and for the weather radar community (e.g., Heistermann et al. 2015). Thirty or more years ago, all algorithms would have been programmed in FORTRAN; with the current existence of algorithms in many languages, code sharing has become more difficult, so adopting a community programming language could also be beneficial. Following the weather radar community, the Python programming language is an attractive candidate for such a package. In any event, the chosen package should be modular so various authors can incorporate enhanced features or extra options as the community's knowledge evolves. It should also be recognized that the development and maintenance of a common processing capability requires resources that are currently not available to any one group, and needs continual maintenance in order to be successful.

In summary, in situ measurements of cloud microphysical properties will remain critical for enhancing process-oriented understanding of clouds, for evaluating models and remote sensing retrievals, and for developing parameterizations for such models and retrievals in the foreseeable future. Although there will always be uncertainties associated with the conversion of raw data to geophysical variables, it is important that future efforts minimize the uncertainties and thoroughly document the assumptions used to obtain those variables so that it is possible to compare data obtained by different groups in a wide range of projects in different geophysical conditions.

Acknowledgments. This research was partially supported by the Office of Science (BER), United States DOE under Grant DE-SC0014065, by the National

Brought to you by University of Alabama in Huntsville | Unauthenticated | Downloaded 02/05/25 05:57 PM UTC

Science Foundation (NSF) under Grants AGS-1213311 and AGS-1359098, and by the DACCIWA project, which has received funding from the European Union Seventh Framework Programme (FP7/2007-2013) under Grant Agreement 603502. The lead author was partially supported by an Advanced Study Program (ASP) visiting faculty fellowship at NCAR during the writing of the manuscript. The comments of seven anonymous reviewers helped clarify the manuscript. The authors would like to thank the many sponsors who have provided funding for the monograph: Leibniz Institute for Tropospheric Research (TROPOS), Forschungszentrum Jülich (FZJ), and Deutsches Zentrum für Luft- und Raumfahrt (DLR), Germany; ETH Zurich, Switzerland; National Center for Atmospheric Research (NCAR), United States; the Met Office, United Kingdom; the University of Illinois, United States; Environment and Climate Change Canada (ECCC), Canada; National Science Foundation (NSF), AGS 1723548, National Aeronautics and Space Administration (NASA), United States; the International Commission on Clouds and Precipitation (ICCP), the European Facility for Airborne Research (EUFAR), and Droplet Measurement Technologies (DMT), United States. NCAR is sponsored by the NSF. Any opinions, findings, and conclusions or recommendations expressed in this publication are those of the author(s) and do not necessarily reflect the views of the National Science Foundation.

APPENDIX A

List of Symbols

A	Habit-dependent coefficient used in m–$D_{\max}$ relations
A_{DOF}	Area corresponding to particles in depth of field
A_p	Projected area of particle
a_1	Coefficient used to characterize base line drift of Nevzorov probe
a_2	Coefficient used to characterize base line drift of Nevzorov probe
b	Habit-dependent coefficient used in m–$D_{\max}$ relations
b'	Fit parameter established in wind tunnel test or flight measurement
b_1	Coefficient used to characterize base line drift of Nevzorov probe
b_2	Coefficient used to characterize base line drift of Nevzorov probe
b_3	Coefficient used to characterize base line drift of Nevzorov probe
c	Specific heat of water
C_f	Adjustment factor for forward-scattering probes
D	Diameter of cylinder
D_A	Mean of L_p and W_p
D_{area}	Area-equivalent diameter
D_H	Hypotenuse of right-angled triangle constructed from L_p and W_p
D_L	Larger of L_p and W_P
D_m	Median mass diameter
$D_{\max}$	Maximum ice crystal dimension
D_S	Diameter of smallest circle enclosing particle measured by imaging probe
G	Parameter used for determining depth of field for imaging probe
K	Ratio of collector to reference power dissipated in cloud-free air
L	Length of cylinder (wire)
L_p	Length of particle measured by OAP along direction of aircraft motion
L_v	Latent heat of vaporization
L^*	Energy required to melt and evaporate measured hydrometers
M	Probe-dependent adjustment factor for forward-scattering probes
M_n	Nth moment of distribution
M_0	Zeroth moment of distribution corresponding to total number concentration
$N(D_{\max})$	Number distribution function
N	Order of moment of distribution
n_m	Number of particles counted in sample interval T
N	Number of photodiodes in a probe
N_a	Total ambient particle number concentration
N_m	Measured particle number concentration
N_0	Shape parameter (intercept) of gamma distribution
P	Air pressure
P_C	Collector power
P_D	Energy lost to the air
P_m	Measured power
P_p	Perimeter of particle
P_R	Reference sensor power
R	Particle radius
r_e	Effective radius
Re	Reynold's number
S	Sensor sample area
SA	Sample area (optical array probe)
SA_E	Extended sample area of forward-scattering probe
SA_Q	Qualified sample area of forward-scattering probe
Sep	Separation of instrument arms

Brought to you by University of Alabama in Huntsville | Unauthenticated | Downloaded 02/05/25 05:57 PM UTC

SV	Sample volume
T	Time of sample period
T_a	Ambient temperature
T_f	Temperature of film
T_S	Average transit time of particles in sample volume
T_w	Constant temperature of wire
V	Velocity of air passing over sensor
V_f	Factor to correct the aircraft velocity to that of the sensor
W	Width or resolution of an individual photodiode
w_i	Ice water content
w_l	Liquid water content
W	Power required to keep wire at constant temperature
W_p	Width of particle measured by OAP aligned along direction of photodiode array
w_t	Total mass content
$w_{t\mathrm{G1}}$	Total mass content from G1 method
$w_{t\mathrm{G2}}$	Total mass content from G2 method
x	Fit parameter established in wind tunnel test or flight measurement
X	Particle width in number of photodiodes
Z	Distance between particle and object plane
Z_d	Parameter upon which the amount of diffraction depends upon
Z_e	Radar reflectivity factor
α	Probe activity
β	Extinction
μ	Fit parameter (shape) of gamma distribution
λ	Particle detection rate
λ_l	Wavelength of laser
Λ	Fit parameter (slope) of gamma distribution
σ	Scattered light measured by forward-scattering instrument
τ	Average transit time of particle in DOF
τ_1	Mode of peak interarrival time corresponding to naturally occurring particles
τ_2	Mode of peak interarrival time corresponding to shattered particles
τ_i	Interarrival time between particles in sample volume
τ_d	Cumulative dead time during sampling period

APPENDIX B

List of Acronyms

2D	Two-dimensional
2DC	Two-dimensional cloud probe
2DP	Two-dimensional precipitation probe
2DS	Two-dimensional stereo probe
ADPAA	Airborne Data Processing and Analysis
BCP	Backscatter Cloud Probe
CAIPEX	Cloud-Aerosol Interaction Precipitation Enhancement Experiment
CAM	Constant altitude method
CAS	Cloud and Aerosol Spectrometer
CAS-POL	CAS with Polarization
CDP	Cloud Droplet Probe
CIP	Cloud Imaging Probe
CIP-G	Cloud Imaging Probe-Gray
CPI	Cloud particle imager
CPSPD	Cloud Particle Spectrometer with Polarization Detection
CSI	Cloud Spectrometer and Impactor Probe
CVI	Counterflow Virtual Impactor
DMT	Droplet Measurement Technologies
DOF	Depth of field
EAW	Effective array width
EUFAR	European Facility for Airborne Research
FAAM	Facility for Airborne Atmospheric Measurements
FCDP	Fast Cloud Droplet Probe
FFSSP	Fast Forward Scattering Spectrometer Probe
FSSP	Forward Scattering Spectrometer Probe
HAIC	High-altitude ice crystals
HIWC	High ice water content
HOLODEC	Holographic Detector for Clouds
HSI	High spectral imager
HVPS3	High Volume Precipitation Sampler 3
IAS	Indicated airspeed
ICCP	International Commission on Clouds and Precipitation
IKP2	Isokinetic Evaporator Probe 2
NCAR	National Center for Atmospheric Research
NOAA	National Oceanic and Atmospheric Administration
OAP	Optical array probe
OASIS	University of Manchester Optical Array Shadow Imaging Software
OPM	Optimum parameterization method
PbP	Particle-by-particle
PHIPS-HALO	Particle Habit Imaging and Polar Scattering Probe
PIP	Precipitation Imaging Probe
PMS	Particle Measuring Systems
PVM	Particle Volume Monitor
RAL	Research Applications Laboratory
SAMAC	Software for Airborne Measurements of Aerosols and Clouds

Brought to you by University of Alabama in Huntsville | Unauthenticated | Downloaded 02/05/25 05:57 PM UTC

SD	Size distribution
SEA	Scientific Engineering Applications
SID	Small Ice Detector
SODA	System for OAP Data Analysis
SPEC	Stratton Park Engineering Company
TAS	True airspeed
TDL	Tunable diode laser
UIOOPS	University of Illinois/Oklahoma Optical Array Probe Processing Software

REFERENCES

Abel, S. J., R. J. Cotton, P. A. Barrett, and A. K. Vance, 2014: A comparison of ice water content measurement techniques on the FAAM BAe-146 aircraft. *Atmos. Meas. Tech.*, **7**, 3007–3022, doi:10.5194/amt-7-3007-2014.

Ackerman, T. P., K. N. Liou, F. P. Valero, and L. Pfister, 1988: Heating rates in tropical anvils. *J. Atmos. Sci.*, **45**, 1606–1623, doi:10.1175/1520-0469(1988)045<1606:HRITA>2.0.CO;2.

Ardanuy, P. E., L. L. Stowe, A. Gruber, and M. Weiss, 1991: Shortwave, longwave, and net cloud-radiative forcing as determined from Nimbus 7 observations. *J. Geophys. Res.*, **96**, 18 537–18 550, doi:10.1029/91JD01992.

Atlas, D., S. Y. Matrosov, A. J. Heymsfield, M. D. Chou, and D. B. Wolff, 1995: Radar and radiation properties of ice clouds. *J. Appl. Meteor.*, **34**, 2329–2345, doi:10.1175/1520-0450(1995)034<2329:RARPOI>2.0.CO;2.

Austin, R. T., A. J. Heymsfield, and G. L. Stephens, 2009: Retrieval of ice cloud microphysical parameters using the CloudSat millimeter-wave radar and temperature. *J. Geophys. Res.*, **114**, D00A23, doi:10.1029/2008JD010049.

Baker, B. A., 1992: Turbulent entrainment and mixing in clouds: A new observational approach. *J. Atmos. Sci.*, **49**, 387–404, doi:10.1175/1520-0469(1992)049<0387:TEAMIC>2.0.CO;2.

——, and R. P. Lawson, 2006: Improvement in determination of ice water content from two-dimensional particle imagery. Part I: Image-to-mass relationships. *J. Appl. Meteor. Climatol.*, **45**, 1282–1290, doi:10.1175/JAM2398.1.

——, A. Korolev, R. P. Lawson, D. O'Connor, and Q. Mo, 2009: Drop size distributions and the lack of small drops in RICO rain shafts. *J. Appl. Meteor. Climatol.*, **48**, 616–623, doi:10.1175/2008JAMC1934.1.

Baran, A. J., 2012: From the single-scattering properties of ice crystals to climate prediction: A way forward. *Atmos. Res.*, **112**, 45–69, doi:10.1016/j.atmosres.2012.04.010.

Battaglia, A., E. Rustemeier, A. Tokay, U. Blahak, and C. Simmer, 2010: PARSIVEL snow observations: A critical assessment. *J. Atmos. Oceanic Technol.*, **27**, 333–344, doi:10.1175/2009JTECHA1332.1.

Baum, B. A., A. J. Heymsfield, P. Yang, and S. T. Bedka, 2005a: Bulk scattering properties for the remote sensing of ice clouds. Part I: Microphysical data and models. *J. Appl. Meteor.*, **44**, 1885–1895, doi:10.1175/JAM2308.1.

——, P. Yang, A. J. Heymsfield, S. Platnick, M. D. King, Y. X. Hu, and S. T. Bedka, 2005b: Bulk scattering properties for the remote sensing of ice clouds. Part II: Narrowband models. *J. Appl. Meteor.*, **44**, 1896–1911, doi:10.1175/JAM2309.1.

——, ——, S. Nasiri, A. K. Heidinger, A. Heymsfield, and J. Li, 2007: Bulk scattering properties for the remote sensing of ice clouds. Part III: High-resolution spectral models from 100 to 3250 cm^{-1}. *J. Appl. Meteor. Climatol.*, **46**, 423–434, doi:10.1175/JAM2473.1.

——, ——, A. J. Heymsfield, C. G. Schmitt, Y. Xie, A. Bansemer, and Z. Zhang, 2011: Improvements in shortwave bulk scattering and absorption models for the remote sensing of ice clouds. *J. Appl. Meteor. Climatol.*, **50**, 1037–1056, doi:10.1175/2010JAMC2608.1.

Baumgardner, D., and J. E. Dye, Eds., 1982: Cloud Particle Measurement Symposium: Summaries and Abstracts. NCAR Tech. Note NCAR/TN-199+PROC, doi:10.5065/D60P0WXP.

——, and ——, 1983: The 1982 Cloud Particle Measurement Symposium. *Bull. Amer. Meteor. Soc.*, **64**, 366–370.

——, and A. Korolev, 1997: Airspeed corrections for optical array probe sample volumes. *J. Atmos. Oceanic Technol.*, **14**, 1224–1229, doi:10.1175/1520-0426(1997)014<1224:ACFOAP>2.0.CO;2.

——, J. W. Strapp, and J. E. Dye, 1985: Evaluation of the forward scattering spectrometer probe. Part II: Corrections for coincidence and dead-time losses. *J. Atmos. Oceanic Technol.*, **2**, 626–632, doi:10.1175/1520-0426(1985)002<0626:EOTFSS>2.0.CO;2.

——, and Coauthors, 2012: In situ, airborne instrumentation: Addressing and solving measurement problems in ice clouds. *Bull. Amer. Meteor. Soc.*, **93**, 29–34, doi:10.1175/BAMS-D-11-00123.1.

——, and Coauthors, 2017: Cloud ice properties: In situ measurement challenges. *Ice Formation and Evolution in Clouds and Precipitation: Measurement and Modeling Challenges, Meteor. Monogr.*, No. 58, Amer. Meteor. Soc., doi:10.1175/AMSMONOGRAPHS-D-16-0011.1.

Beswick, K., D. Baumgardner, M. Gallagher, A. Volz-Thomas, P. Nedelec, K.-Y. Wang, and S. Lance, 2014:The backscatter cloud probe—A compact low-profile autonomous optical spectrometer. *Atmos. Meas. Tech.*, **7**, 1443–1457, doi:10.5194/amt-7-1443-2014.

——, and Coauthors, 2015: Properties of small cirrus ice crystals from commercial aircraft measurements and implications for flight operations. *Tellus*, **67B**, 27876, doi:10.3402/tellusb.v67.27876.

Borrmann, S., B. Luot, and M. Mishchenko, 2000: Application of the T-matrix method to the measurement of aspherical (ellipsoidal) particles with forward scattering optical particle counters. *J. Aerosol Sci.*, **31**, 789–799, doi:10.1016/S0021-8502(99)00563-7.

Boudala, F. S., G. A. Isaac, Q. Fu, and S. G. Cober, 2002: Parameterization of effective ice particle size for high-latitude clouds. *Int. J. Climatol.*, **22**, 1267–1284, doi:10.1002/joc.774.

——, ——, and D. Hudak, 2006: Ice water content and precipitation rate as a function of equivalent radar reflectivity and temperature based on in situ observations. *J. Geophys. Res.*, **111**, D11202, doi:10.1029/2005JD006499.

Brenguier, J.-L., 1989: Coincidence and dead-time corrections for particles counters. Part II: High concentration measurements with an FSSP. *J. Atmos. Oceanic Technol.*, **6**, 585–598, doi:10.1175/1520-0426(1989)006<0585:CADTCF>2.0.CO;2.

——, and L. Amodei, 1989: Coincidence and dead-time corrections for particle counters. Part I: A general mathematical formalism. *J. Atmos. Oceanic Technol.*, **6**, 575–584, doi:10.1175/1520-0426(1989)006<0575:CADTCF>2.0.CO;2.

——, D. Baumgardner, and B. Baker, 1994: A review and discussion of processing algorithms for FSSP concentration measurements. *J. Atmos. Oceanic Technol.*, **11**, 1409–1414, doi:10.1175/1520-0426(1994)011<1409:ARADOP>2.0.CO;2.

——, and Coauthors, 2013: In situ measurements of cloud and precipitation particles. *Airborne Measurements for Environmental Research*, J.-L. Brenguier and M. Wendisch, Eds., Wiley, 239–324.

Brown, P. R., and P. N. Francis, 1995: Improved measurements of the ice water content in cirrus using a total-water probe.

Brought to you by University of Alabama in Huntsville | Unauthenticated | Downloaded 02/05/25 05:57 PM UTC

J. Atmos. Oceanic Technol., **12**, 410–414, doi:10.1175/1520-0426(1995)012<0410:IMOTIW>2.0.CO;2.

Cerni, T. A., 1983: Determination of the size and concentration of cloud drops with an FSSP. *J. Climate Appl. Meteor.*, **22**, 1346–1355, doi:10.1175/1520-0450(1983)022<1346:DOTSAC>2.0.CO;2.

Cober, S. G., G. A. Isaac, A. V. Korolev, and J. W. Strapp, 2001: Assessing cloud-phase conditions. *J. Appl. Meteor.*, **40**, 1967–1983, doi:10.1175/1520-0450(2001)040<1967:ACPC>2.0.CO;2.

Collier, C. T., E. Hesse, L. Taylor, Z. Ulanowski, A. Penttila, and T. Nousiainen, 2016: Effects of surface roughness with two scales on light scattering by hexagonal ice crystals large compared to the wavelength: DDA results. *J. Quant. Spectrosc. Radiat. Transfer*, **182**, 225–239, doi:10.1016/j.jqsrt.2016.06.007.

Cooper, W. A., 1978: Cloud physics investigation by the University of Wyoming in HIPLEX 1977. Bureau of Reclamation Rep. AS 119, 321 pp.

——, 1988: Effects of coincidence on measurements with a forward scattering spectrometer probe. *J. Atmos. Oceanic Technol.*, **5**, 823–832, doi:10.1175/1520-0426(1988)005<0823:EOCOMW>2.0.CO;2.

——, and D. Baumgardner, 1988: Meeting Review: Workshop on Airborne Instrumentation 19-21 October 1988. NCAR Tech. Note NCAR/TN-330+PROC, doi:10.5065/D61C1TT3.

Cotton, R., S. Osborne, Z. Ulanowski, E. Hirst, P. H. Kaye, and R. S. Greenaway, 2010: The ability of the Small Ice Detector (SID-2) to characterize cloud particle and aerosol morphologies obtained during flights of the FAAM BAe-146 research aircraft. *J. Atmos. Oceanic Technol.*, **27**, 290–303, doi:10.1175/2009JTECHA1282.1.

Davis, A. B., A. Marshak, H. Gerber, and W. J. Wiscombe, 1999: Horizontal structure of marine boundary-layer clouds from cm to km scales. *J. Geophys. Res.*, **104**, 6123–6144, doi:10.1029/1998JD200078.

Davis, S. M., L. M. Avallone, E. M. Weinstock, C. H. Twohy, J. B. Smith, and G. L. Kok, 2007: Comparisons of in situ measurements of cirrus cloud ice water content. *J. Geophys. Res.*, **112**, D10212, doi:10.1029/2006JD008214.

Davison, C., J. MacLeod, J. Strapp, and D. Buttsworth, 2009: Isokinetic total water content probe in a naturally aspirating configuration: Initial aerodynamic design and testing. *46th AIAA Aerospace Sciences Meeting and Exhibit*, Reno, NV, American Institute of Aeronautics and Astronautics, doi:10.2514/6.2008-435.

Delanoë, J., A. Protat, D. Bouniol, A. Heymsfield, A. Bansemer, and P. Brown, 2007: The characterization of ice cloud properties from Doppler radar measurements. *J. Appl. Meteor. Climatol.*, **46**, 1682–1698, doi:10.1175/JAM2543.1.

Deng, M., and G. G. Mace, 2006: Cirrus microphysical properties and air motion statistics using cloud radar Doppler moments. Part I: Algorithm description. *J. Appl. Meteor. Climatol.*, **45**, 1690–1709, doi:10.1175/JAM2433.1.

——, ——, Z. Wang, and R. P. Lawson, 2013: Evaluation of several A-Train ice cloud retrieval products with in situ measurements collected during the SPARTICUS campaign. *J. Appl. Meteor. Climatol.*, **52**, 1014–1030, doi:10.1175/JAMC-D-12-054.1.

Donovan, D. P., and A. C. A. P. van Lammeren, 2001: Cloud effective particle size and water content profile retrievals using combined lidar and radar observations: 1. Theory and examples. *J. Geophys. Res.*, **106**, 27 425–27 448, doi:10.1029/2001JD900243.

Dudhia, J., 1989: Nuerical study of convection observed during the winter monsoon experiment using a mesoscale two-dimensional model. *J. Atmos. Sci.*, **46**, 3077–3107, doi:10.1175/1520-0469(1989)046<3077:NSOCOD>2.0.CO;2.

Duroure, C., 1982: Une nouvelle metode de traitment des images d'hydrometeores données par les sondes bidimensionelles. *J. Rech. Atmos.*, **6**, 71–84.

Dye, J. E., and D. Baumgardner, 1984: Evaluation of the Forward Scattering Spectrometer Probe. Part I: Electronic and optical studies. *J. Atmos. Oceanic Technol.*, **1**, 329–344, doi:10.1175/1520-0426(1984)001<0329:EOTFSS>2.0.CO;2.

Febvre, G., J. F. Gayet, V. Scherbakov, C. Gourbeyre, and O. Jourdan, 2012: Some effects of ice crystals on the FSSP measurements in mixed-phase clouds. *Atmos. Chem. Phys.*, **12**, 8963–8977, doi:10.5194/acp-12-8963-2012.

Ferrier, B. S., 1994: A double-moment multiple-phase four-class bulk ice scheme. Part I: Description. *J. Atmos. Sci.*, **51**, 249–280, doi:10.1175/1520-0469(1994)051<0249:ADMMPF>2.0.CO;2.

Field, P. R., and A. J. Heymsfield, 2003: Aggregation and scaling of ice crystal size distributions. *J. Atmos. Sci.*, **60**, 544–560, doi:10.1175/1520-0469(2003)060<0544:AASOIC>2.0.CO;2.

——, and ——, 2015: Importance of snow to global precipitation. *Geophys. Res. Lett.*, **42**, 9512–9520, doi:10.1002/2015GL065497.

——, R. Wood, P. R. A. Brown, P. H. Kaye, E. Hirst, R. Greenaway, and J. A. Smith, 2003: Ice particle interarrival times measured with a fast FSSP. *J. Atmos. Oceanic Technol.*, **20**, 249–261, doi:10.1175/1520-0426(2003)020<0249:IPITMW>2.0.CO;2.

——, A. J. Heymsfield, and A. Bansemer, 2006: Shattering and particle interarrival times measured by optical array probes in ice clouds. *J. Atmos. Oceanic Technol.*, **23**, 1357–1371, doi:10.1175/JTECH1922.1.

——, ——, and ——, 2007: Snow size distribution parameterization for midlatitude and tropical ice clouds. *J. Atmos. Sci.*, **64**, 4346–4365, doi:10.1175/2007JAS2344.1.

——, and Coauthors, 2017: Secondary ice production: Current state of the science and recommendations for the future. *Ice Formation and Evolution in Clouds and Precipitation: Measurement and Modeling Challenges*, *Meteor. Monogr.*, No. 58, Amer. Meteor. Soc., doi:10.1175/AMSMONOGRAPHS-D-16-0014.1.

Finlon, J. A., G. M. McFarquhar, R. M. Rauber, D. M. Plummer, B. F. Jewett, D. Leon, and K. R. Knupp, 2016: A comparison of X-band polarization parameters with in situ microphysical measurements in the comma head of two winter cyclones. *J. Appl. Meteor. Climatol.*, **55**, 2549–2574, doi:10.1175/JAMC-D-16-0059.1.

Fontaine, E., A. Schwarzenboeck, J. Delanoë, W. Wobrock, D. Leroy, R. Dupuy, C. Gourbeyre, and A. Protat, 2014: Constraining mass–diameter relations from hydrometeor images and cloud radar reflectivities in tropical continental and oceanic convective anvils. *Atmos. Chem. Phys.*, **14**, 11 367–11 392, doi:10.5194/acp-14-11367-2014.

Fouilloux, A., J. Iaquinta, C. Duroure, and F. Albers, 1997: A statistical analysis for pattern recognition of small cloud particles sampled with a PMS OAP-2DC probe. *Ann. Geophys.*, **15**, 840–846, doi:10.1007/s00585-997-0840-5.

Frisch, S., M. Shupe, I. Djalalova, G. Feingold, and M. Poellot, 2002: The retrieval of stratus cloud droplet effective radius with cloud radars. *J. Atmos. Oceanic Technol.*, **19**, 835–842, doi:10.1175/1520-0426(2002)019<0835:TROSCD>2.0.CO;2.

Fu, Q., 1996: An accurate parameterization of the solar radiative properties of cirrus clouds for climate models. *J. Climate*, **9**, 2058–2082, doi:10.1175/1520-0442(1996)009<2058:AAPOTS>2.0.CO;2.

Gagne, S., L. P. MacDonald, W. R. Leaitch, and J. R. Pierce, 2016: Software to analyze the relationship between aerosol, clouds and precipitation: SAMAC. *Atmos. Meas. Tech.*, **9**, 619–630, doi:10.5194/amt-9-619-2016.

Brought to you by University of Alabama in Huntsville | Unauthenticated | Downloaded 02/05/25 05:57 PM UTC

Gardiner, B. A., and J. Hallett, 1985: Degradation of in-cloud Forward Scattering Spectrometer Probe measurements in the presence of ice particles. *J. Atmos. Oceanic Technol.*, **2**, 171–180, doi:10.1175/1520-0426(1985)002<0171:DOICFS>2.0.CO;2.

Gayet, J.-F., 1976: Sur les performances de L'ASSP-100 de Knollenberg pour la granulometrie des nuages. *J. Rech. Atmos.*, **10**, 105–118.

——, P. R. A. Brown, and F. Albers, 1993: A comparison of in-cloud measurements obtained with six PMS 2D-C probes. *J. Atmos. Oceanic Technol.*, **10**, 180–194, doi:10.1175/1520-0426(1993)010<0180:ACOICM>2.0.CO;2.

——, G. Febvre, and H. Larsen, 1996: The reliability of the PMS FSSP in the presence of small ice crystals. *J. Atmos. Oceanic Technol.*, **13**, 1300–1310, doi:10.1175/1520-0426(1996)013<1300:TROTPF>2.0.CO;2.

Gerber, H., B. Arends, and A. Ackerman, 1994: New microphysics sensor for aircraft use. *Atmos. Res.*, **31**, 235–252, doi:10.1016/0169-8095(94)90001-9.

Gilmore, M. S., J. M. Straka, and E. N. Rasmussen, 2004: Precipitation uncertainty due to variations in precipitation particle parameters within a simple microphysics scheme. *Mon. Wea. Rev.*, **132**, 2610–2627, doi:10.1175/MWR2810.1.

Grim, J. A., G. M. McFarquhar, R. M. Rauber, A. M. Smith, and B. F. Jewett, 2009: Microphysical and thermodynamic structure and evolution of the trailing stratiform regions of mesoscale convective systems during BAMEX. Part II: Column model simulations. *Mon. Wea. Rev.*, **137**, 1186–1205, doi:10.1175/2008MWR2505.1.

Hallett, J., 2003: Measurement in the atmosphere. *Handbook of Weather, Climate and Water: Dynamics, Climate, Physical Meteorology, Weather Systems, and Measurements*, T. D. Potter and B. R. Colman, Eds., Wiley-Interscience, 711–720.

Harrington, J. Y., K. Sulia, and H. Morrison, 2013a: A method for adaptive habit prediction in bulk microphysical models. Part I: Theoretical development. *J. Atmos. Sci.*, **70**, 349–364, doi:10.1175/JAS-D-12-040.1.

——, ——, and ——, 2013b: A method for adaptive habit prediction in bulk microphysical models. Part II: Parcel model corroboration. *J. Atmos. Sci.*, **70**, 365–376, doi:10.1175/JAS-D-12-0152.1.

Hayman, M., K. J. McMenamin, and J. B. Jensen, 2016: Response time characteristics of the Fast-2D optical array probe detector board. *J. Atmos. Oceanic Technol.*, **33**, 2569–2583, doi:10.1175/JTECH-D-16-0062.1.

Heistermann, M., and Coauthors, 2015: Source software for the weather radar community. *Bull. Amer. Meteor. Soc.*, **96**, 117–128, doi:10.1175/BAMS-D-13-00240.1.

Heymsfield, A. J., 2003: Properties of tropical and midlatitude ice cloud particle ensembles. Part I: Median mass diameters and terminal velocities. *J. Atmos. Sci.*, **60**, 2573–2591, doi:10.1175/1520-0469(2003)060<2573:POTAMI>2.0.CO;2.

——, 2007: On measurements of small ice crystals in clouds. *Geophys. Res. Lett.*, **34**, L23812, doi:10.10292007GL030951.

——, and J. L. Parrish, 1979: Techniques employed in the processing of particle size spectra and state parameter data obtained with T-28 aircraft platform. NCAR Tech. Note NCAR/TN-137+1A0, 78 pp.

——, and C. M. R. Platt, 1984: A parameterization of the particle size spectrum of ice clouds in terms of the ambient temperature and the ice water content. *J. Atmos. Sci.*, **41**, 846–855, doi:10.1175/1520-0469(1984)041<0846:APOTPS>2.0.CO;2.

——, and D. Baumgardner, 1985: Summary of a workshop on processing 2D probe data. *Bull. Amer. Meteor. Soc.*, **66**, 437–440.

——, and L. M. Miloshevich, 1991: Limit to greenhouse warming? *Nature*, **351**, 14–15, doi:10.1038/351014a0.

——, and G. M. McFarquhar, 2002: Mid-latitude and tropical cirrus: Microphysical properties. *Cirrus*, D. K. Lynch et al., Eds., Oxford University Press, 78–101.

——, A. Bansemer, P. R. Field, S. L. Durden, J. L. Stith, J. E. Dye, W. Hall, and C. A. Grainger, 2002a: Observations and parameterizations of particle size distributions in deep tropical cirrus and stratiform precipitating clouds: Results from in situ observations in TRMM field campaigns. *J. Atmos. Sci.*, **59**, 3457–3491, doi:10.1175/1520-0469(2002)059<3457:OAPOPS>2.0.CO;2.

——, S. Lewis, A. Bansemer, J. Iaquinta, L. M. Miloshevich, M. Kajikawa, C. Twohy, and M. R. Poellot, 2002b: A general approach for deriving the properties of cirrus and stratiform ice cloud particles. *J. Atmos. Sci.*, **59**, 3–29, doi:10.1175/1520-0469(2002)059<0003:AGAFDT>2.0.CO;2.

——, A. Bansemer, S. Schmidt, C. Twohy, and M. Poellot, 2004: Effective ice particle densities derived from aircraft data. *J. Atmos. Sci.*, **61**, 982–994, doi:10.1175/1520-0469(2004)061<0982:EIPDDF>2.0.CO;2.

——, C. Schmitt, A. Bansemer, G. J. van Zadelhoff, M. R. J. McGill, C. Twohy, and D. Baumgardner, 2006: Effective radius of icecloud particle populations derived from aircraft probes. *J. Atmos. Oceanic Technol.*, **23**, 361–380, doi:10.1175/JTECH1857.1.

——, ——, ——, and C. Twohy, 2010: Improved representation of ice particle masses based on observations in natural clouds. *J. Atmos. Sci.*, **67**, 3303–3318, doi:10.1175/2010JAS3507.1.

Hobbs, P. V., A. L. Rangno, M. Shupe, and T. Uttal, 2001: Airborne studies of cloud structures over the Arctic Ocean and comparisons with retrievals from ship-based remote sensing measurements. *J. Geophys. Res.*, **106**, 15 029–15 044, doi:10.1029/2000JD900323.

Hogan, R. J., M. P. Mittermaier, and A. J. Illingworth, 2006: The retrieval of ice water content from radar reflectivity factor and temperature and its use in evaluating a mesoscale model. *J. Appl. Meteor. Climatol.*, **45**, 301–317, doi:10.1175/JAM2340.1.

Holroyd, E. W., 1987: Some techniques and uses of 2D-C habit classification for snow particles. *J. Atmos. Oceanic Technol.*, **4**, 498–511, doi:10.1175/1520-0426(1987)004<0498:STAUOC>2.0.CO;2.

Hunter, H. E., R. M. Dyer, and M. Glass, 1984: A two-dimensional hydrometeor classifier derived from observed data. *J. Atmos. Oceanic Technol.*, **1**, 28–36, doi:10.1175/1520-0426(1984)001<0028:ATDHMC>2.0.CO;2.

Isaac, G. A., and K. S. Schmidt, 2009: Cloud properties from in-situ and remote sensing measurements: Capability and limitations. *Clouds in the Perturbed Climate System*, J. Heintzenberg and R. J. Charlson, Eds., MIT Press, 73–106.

Ivanova, D., D. L. Mitchell, W. P. Arnott, and M. Poellot, 2001: A GCM parameterization for bimodal size spectra and ice mass removal rates in mid-latitude cirrus clouds. *Atmos. Res.*, **59**, 89–113, doi:10.1016/S0169-8095(01)00111-9.

Jackson, R. C., and G. M. McFarquhar, 2014: An assessment of the impact of antishattering tips and artifact removal techniques on bulk cloud ice microphysical and optical properties measured by the 2D cloud probe. *J. Atmos. Oceanic Technol.*, **31**, 2131–2144, doi:10.1175/JTECH-D-14-00018.1.

——, and Coauthors, 2012: The dependence of ice microphysics on aerosol concentration in Arctic mixed-phase stratus clouds during ISDAC and M-PACE. *J. Geophys. Res.*, **117**, D15207, doi:10.1029/2012JD017668.

——, G. M. McFarquhar, J. Stith, M. Beals, R. A. Shaw, J. Jensen, J. Fugal, and A. Korolev, 2014: An assessment of the impact

Brought to you by University of Alabama in Huntsville | Unauthenticated | Downloaded 02/05/25 05:57 PM UTC

of antishattering tips and artifact removal techniques on cloud ice size distributions measured by the 2D cloud probe. *J. Atmos. Oceanic Technol.*, **31**, 2567–2590, doi:10.1175/JTECH-D-13-00239.1.

Jensen, E. J., and Coauthors, 2009: On the importance of small ice crystals in tropical anvil cirrus. *Atmos. Chem. Phys.*, **9**, 5519–5537, doi:10.5194/acp-9-5519-2009.

Joe, P., and R. List, 1987: Testing and performance of two-dimensional optical array spectrometer with grey scale. *J. Atmos. Oceanic Technol.*, **4**, 139–150, doi:10.1175/1520-0426(1987)004<0139:TAPOTD>2.0.CO;2.

Katsuhiro, K., and Coauthors, 2013: A global classification of snow crystals, ice crystals, and solid precipitation based on observations from middle latitudes to polar regions. *Atmos. Res.*, **132–133**, 460–472, doi:10.1016/j.atmosres.2013.06.006.

King, W. D., 1984: Air flow and particle trajectories around aircraft fuselages. I: Theory. *J. Atmos. Oceanic Technol.*, **1**, 5–13, doi:10.1175/1520-0426(1984)001<0005:AFAPTA>2.0.CO;2.

——, 1985: Air flow and particle trajectories around aircraft fuselages. Part III: Extensions to particles of arbitrary shape. *J. Atmos. Oceanic Technol.*, **2**, 539–547, doi:10.1175/1520-0426(1985)002<0539:AFAPTA>2.0.CO;2.

——, D. A. Parkin, and R. J. Handsworth, 1978: A hot-wire liquid water device having fully calculable response characteristics. *J. Appl. Meteor.*, **17**, 1809–1813, doi:10.1175/1520-0450(1978)017<1809:AHWLWD>2.0.CO;2.

——, D. E. Turvey, D. Williams, and D. J. Llewellyn, 1984: Air flow and particle trajectories around aircraft fuselages. II: Measurements. *J. Atmos. Oceanic Technol.*, **1**, 14–21, doi:10.1175/1520-0426(1984)001<0014:AFAPTA>2.0.CO;2.

Knollenberg, R. G., 1970: The optical array: An alternative to scattering or extinction for airborne particle size determination. *J. Appl. Meteor.*, **9**, 86–103, doi:10.1175/1520-0450(1970)009<0086:TOAAAT>2.0.CO;2.

Korolev, A. V., 2007: Reconstruction of the sizes of spherical particles from their shadow images. Part I: Theoretical considerations. *J. Atmos. Oceanic Technol.*, **24**, 376–389, doi:10.1175/JTECH1980.1.

——, and B. Sussman, 2000: A technique for habit classification of cloud particles. *J. Atmos. Oceanic Technol.*, **17**, 1048–1057, doi:10.1175/1520-0426(2000)017<1048:ATFHCO>2.0.CO;2.

——, and G. Isaac, 2003: Roundness and aspect ratio of particles in ice clouds. *J. Atmos. Sci.*, **60**, 1795–1808, doi:10.1175/1520-0469(2003)060<1795:RAAROP>2.0.CO;2.

——, and ——, 2005: Shattering during sampling by OAPs and HVPS. Part I: Snow particles. *J. Atmos. Oceanic Technol.*, **22**, 528–542, doi:10.1175/JTECH1720.1.

——, and P. Field, 2015: Assessment of performance of the inter-arrival time algorithm to identify ice shattering artifacts in cloud particle probes measurements. *Atmos. Meas. Tech.*, **8**, 761–777, doi:10.5194/amt-8-761-2015.

——, S. V. Kuznetsov, Y. E. Makarov, and V. S. Novikov, 1991: Evaluation of measurements of particle size and sample area from optical array probes. *J. Atmos. Oceanic Technol.*, **8**, 514–522, doi:10.1175/1520-0426(1991)008<0514:EOMOPS>2.0.CO;2.

——, J. W. Strapp, G. A. Isaac, and A. N. Nevzorov, 1998a: The Nevzorov airborne hot-wire LWC-TWC probe: Principle of operation and performance characteristics. *J. Atmos. Oceanic Technol.*, **15**, 1495–1510, doi:10.1175/1520-0426(1998)015<1495:TNAHWL>2.0.CO;2.

——, ——, and ——, 1998b: Evaluation of the accuracy of PMS optical array probes. *J. Atmos. Oceanic Technol.*, **15**, 708–720, doi:10.1175/1520-0426(1998)015<0708:EOTAOP>2.0.CO;2.

——, G. A. Isaac, and J. Hallett, 1999: Ice particle habits in Arctic clouds. *Geophys. Res. Lett.*, **26**, 1299–1302, doi:10.1029/1999GL900232.

——, E. F. Emery, J. W. Strapp, S. G. Cober, G. A. Isaac, M. Wasey, and D. Marcotte, 2011: Small ice particles in tropospheric clouds: Fact or artifact? *Bull. Amer. Meteor. Soc.*, **92**, 967–973, doi:10.1175/2010BAMS3141.1.

——, ——, and K. Creelman, 2013a: Modification and tests of particle probe tips to mitigate effects of ice shattering. *J. Atmos. Oceanic Technol.*, **30**, 690–708, doi:10.1175/JTECH-D-12-00142.1.

——, ——, J. W. Strapp, S. G. Cober, and G. A. Isaac, 2013b: Quantification of the effects of shattering on airborne ice particle measurements. *J. Atmos. Oceanic Technol.*, **30**, 2527–2553, doi:10.1175/JTECH-D-13-00115.1.

——, J. W. Strapp, G. A. Isaac, and E. Emery, 2013c: Improved airborne hot-wire measurements of ice water content in clouds. *J. Atmos. Oceanic Technol.*, **30**, 2121–2131, doi:10.1175/JTECH-D-13-00007.1.

——, and Coauthors, 2017: Mixed-phase clouds: Progress and challenges. *Ice Formation and Evolution in Clouds and Precipitation: Measurement and Modeling Challenges, Meteor. Monogr.*, No. 58, Amer. Meteor. Soc., doi:10.1175/AMSMONOGRAPHS-D-17-0001.1.

Kostinski, A. B., and A. R. Jameson, 1997: Fluctuation properties of precipitation. Part I: Derivations of single size drop counts from the Poisson distribution. *J. Atmos. Sci.*, **54**, 2174–2186, doi:10.1175/1520-0469(1997)054<2174:FPOPPI>2.0.CO;2.

——, and ——, 2000: On the spatial distribution of cloud particles. *J. Atmos. Sci.*, **57**, 901–915, doi:10.1175/1520-0469(2000)057<0901:OTSDOC>2.0.CO;2.

Krämer, M., C. Twohy, M. Hermann, A. Afchine, S. Dhaniyala and A Korolev, 2013: Aerosol and cloud particle sampling. *Airborne Measurements: Methods and Instruments*, M. Wendisch and J.-L. Brenguier, Eds., Wiley, 303–342.

——, and Coauthors, 2016: A microphysics guide to cirrus clouds—Part 1: Cirrus types. *Atmos. Chem. Phys.*, **16**, 3463–3483, doi:10.5194/acp-16-3463-2016.

Kristjansson, J. E., J. M. Edwards, and D. L. Mitchell, 2000: Impact of a new scheme for optical properties of ice crystals on climates of two GCMs. *J. Geophys. Res.*, **105**, 10 063–10 079, doi:10.1029/2000JD900015.

Kulie, M. S., and R. Bennartz, 2009: Utilizing spaceborne radars to retrieve dry snowfall. *J. Appl. Meteor. Climatol.*, **48**, 2564–2580, doi:10.1175/2009JAMC2193.1.

Lance, S., 2012: Coincidence errors in a cloud droplet probe (CDP) and a cloud and aerosol spectrometer (CAS), and the improved performance of a modified CDP. *J. Atmos. Oceanic Technol.*, **29**, 1532–1541, doi:10.1175/JTECH-D-11-00208.1.

——, C. A. Brock, D. Rogers, and J. A. Gordon, 2010: Water droplet calibration of the cloud droplet probe (CDP) and in-flight performance in liquid, ice and mixed phase clouds during ARCPAC. *Atmos. Meas. Tech.*, **3**, 1683–1706, doi:10.5194/amt-3-1683-2010.

Larsen, H., J.-F. Gayet, G. Febvre, H. Chepfer, and G. Brogniez, 1998: Measurement errors in cirrus cloud microphysical properties. *Ann. Geophys.*, **16**, 266–276, doi:10.1007/s00585-998-0266-8.

Lawson, R. P., 2011: Effects of ice particles shattering on the 2D-S probe. *Atmos. Meas. Tech.*, **4**, 1361–1381, doi:10.5194/amt-4-1361-2011.

——, B. A. Baker, C. G. Schmitt, and T. L. Jensen, 2001: An overview of microphysical properties of Arctic clouds observed in May and July 1998 during FIRE ACE. *J. Geophys. Res.*, **106**, 14 989–15 014, doi:10.1029/2000JD900789.

——, D. O'Connor, P. Zmarzly, K. Weaver, B. Baker, Q. Mo, and H. Jonsson, 2006: The 2D-S (Stereo) probe: Design and preliminary tests of a new airborne, high-speed, high-resolution

Brought to you by University of Alabama in Huntsville | Unauthenticated | Downloaded 02/05/25 05:57 PM UTC

particle imaging probe. *J. Atmos. Oceanic Technol.*, **23**, 1462–1477, doi:10.1175/JTECH1927.1.

Leroy, D., E. Fontaine, A. Schwarzenboeck, and J. W. Strapp, 2017: Ice crystal sizes in high ice water content clouds. Part I: Mass–size relationships derived from particle images and TWC for various crystal diameter definitions and impact on median mass diameter. *J. Atmos. Oceanic Technol.*, **34**, 117–136, doi:10.1175/JTECH-D-15-0246.1.

Lilie, L., E. Emery, J. W. Strapp, and J. Emery, 2004: A multiwire hot-wire device for measurement of icing severity, total water content, liquid water content, and droplet diameter. *43rd AIAA Aerospace Sciences Meeting and Exhibit*, Reno, NV, American Institute of Aeronautics and Astronautics, AIAA-2005-859, doi:10.2514/6.2005-859.

Lindqvist, H., K. Muinonen, T. Nousiainen, J. Um, G. M. McFarquhar, P. Haapanala, R. Makkonen, and H. Hakkarainen, 2012: Ice-cloud particle habit classification using principal components. *J. Geophys. Res.*, **117**, D16206, doi:10.1029/2012JD017573.

Liou, K. N., Y. Gu, Q. Yue, and G. M. McFarquhar, 2008: On the correlation between ice water content and ice crystal size and its application to radiative transfer and general circulation models. *Geophys. Res. Lett.*, **35**, L13805, doi:13810.11029/12008GL033918.

Locatelli, J. D., and P. V. Hobbs, 1974: Fall speeds and masses of solid precipitation particles. *J. Geophys. Res.*, **79**, 2185–2197, doi:10.1029/JC079i015p02185.

Mace, G. G., A. J. Heymsfield, and M. R. Poellot, 2002: On retrieving the microphysical properties of cirrus clouds using the moments of the millimeter-wavelength Doppler spectrum. *J. Geophys. Res.*, **107**, 4815, doi:4810.1029/2001JD001308.

Macke, A., J. Mueller, and E. Raschke, 1996: Single scattering properties of atmospheric ice crystals. *J. Atmos. Sci.*, **53**, 2813–2825, doi:10.1175/1520-0469(1996)053<2813:SSPOAI>2.0.CO;2.

Magee, N. B., A. Miller, M. Amaral, and A. Cumiskey, 2014: Mesoscopic surface roughness of ice crystals pervasive across a wide range of ice crystal conditions. *Atmos. Chem. Phys.*, **14**, 12 357–12 371, doi:10.5194/acp-14-12357-2014.

Magono, C., and C. W. Lee, 1966: Meteorological classification of natural snow crystals. *J. Fac. Sci. Hokkaido Univ. Ser. 7*, **2**, 321–335.

Markowski, G. R., 1987: Improving Twomey's algorithm for inversion of aerosol measurement data. *Aerosol Sci. Technol.*, **7**, 127–141, doi:10.1080/02786828708959153.

May, P. T., J. H. Mather, G. Vaughan, K. N. Bower, C. Jakob, G. M. McFarquhar, and G. G. Mace, 2008: The Tropical Warm Pool International Cloud Experiment. *Bull. Amer. Meteor. Soc.*, **89**, 629–645, doi:10.1175/BAMS-89-5-629.

McFarquhar, G. M., 2001: Comments on 'Parametrization of effective sizes of cirrus-cloud particles and its verification against observations' by Zhian Sun and Lawrie Rikus. October B, 1999, 125, 3037–3055. *Quart. J. Roy. Meteor. Soc.*, **127**, 261–265, doi:10.1002/qj.49712757115.

——, and A. J. Heymsfield, 1996: Microphysical characteristics of three cirrus anvils sampled during the Central Equatorial Pacific Experiment. *J. Atmos. Sci.*, **53**, 2401–2423, doi:10.1175/1520-0469(1996)053<2401:MCOTAS>2.0.CO;2.

——, and ——, 1997: Parameterization of tropical cirrus ice crystal size distributions and implications for radiative transfer: Results from CEPEX. *J. Atmos. Sci.*, **54**, 2187–2200, doi:10.1175/1520-0469(1997)054<2187:POTCIC>2.0.CO;2.

——, ——, A. Macke, J. Iaquinta, and S. M. Aulenbach, 1999: Use of observed ice crystal sizes and shapes to calculate mean scattering properties and multispectral radiances: CEPEX April 4, 1993 case study. *J. Geophys. Res.*, **104**, 31 763–31 779, doi:10.1029/1999JD900802.

——, P. Yang, A. Macke, and A. J. Baran, 2002: A new parameterization of single scattering solar radiative properties for tropical anvils using observed ice crystal size and shape distributions. *J. Atmos. Sci.*, **59**, 2458–2478, doi:10.1175/1520-0469(2002)059<2458:ANPOSS>2.0.CO;2.

——, S. Iacobellis, and R. C. Somerville, 2003: SCM simulations of tropical ice clouds using observationally based parameterizations of microphysics. *J. Climate*, **16**, 1643–1664, doi:10.1175/1520-0442(2003)016<1643:SSOTIC>2.0.CO;2.

——, M. S. Timlin, R. M. Rauber, B. F. Jewett, J. A. Grim, and D. P. Jorgensen, 2007a: Vertical variability of cloud hydrometeors in the stratiform region of mesoscale convective systems and bow echoes. *Mon. Wea. Rev.*, **135**, 3405–3428, doi:10.1175/MWR3444.1.

——, J. Um, M. Freer, D. Baumgardner, G. L. Kok, and G. G. Mace, 2007b: Importance of small ice crystals to cirrus properties: Observations from the Tropical Warm Pool International Cloud Experiment (TWP-ICE). *Geophys. Res. Lett.*, **34**, L13803, doi:10.1029/2007GL029865.

——, B. Schmid, A. Korolev, J. A. Ogren, P. B. Russell, J. Tomlinson, D. D. Turner, and W. Wiscombe, 2011a: Airborne instrumentation needs for climate and atmospheric research. *Bull. Amer. Meteor. Soc.*, **92**, 1193–1196, doi:10.1175/2011BAMS3180.1.

——, and Coauthors, 2011b: Indirect and Semi-Direct Aerosol Campaign: The impact of Arctic aerosols on clouds. *Bull. Amer. Meteor. Soc.*, **92**, 183–201, doi:10.1175/2010BAMS2935.1.

——, T. Hsieh, M. Freer, J. Mascio, and B. F. Jewett, 2015: The characterization of ice hydrometeor gamma size distributions as volumes in N0–λ–μ phase space: Implications for microphysical process modeling. *J. Atmos. Sci.*, **72**, 892–909, doi:10.1175/JAS-D-14-0011.1.

Meyer, J., 2013: Ice crystal measurements with the new particle spectrometer NIXE-CAPS. *Schr. Forschungszent. Juelich Reihe Umwelt/Environ.*, **160**, http://juser.fz-juelich.de/record/22871/files/FZJ-22871.pdf.

Meyers, M. P., R. L. Walko, J. Y. Harrington, and W. R. Cotton, 1997: New RAMS cloud microphysics parameterization. Part II. The two-moment scheme. *Atmos. Res.*, **45**, 3–39, doi:10.1016/S0169-8095(97)00018-5.

Milbrandt, J. A., and M. K. Yau, 2005: A multimoment bulk microphysics parameterization. Part I: Analysis of the role of the spectral shape parameter. *J. Atmos. Sci.*, **62**, 3051–3064, doi:10.1175/JAS3534.1.

Mitchell, D. L., 1996: Use of mass- and area-dimensional power laws for determining precipitation particle terminal velocities. *J. Atmos. Sci.*, **53**, 1710–1723, doi:10.1175/1520-0469(1996)053<1710:UOMAAD>2.0.CO;2.

——, R. P. Lawson, and B. Baker, 2011a: Understanding effective diameter and its application to terrestrial radiation in ice clouds. *Atmos. Chem. Phys.*, **11**, 3417–3429, doi:10.5194/acp-11-3417-2011.

——, S. Mishra, and R. P. Lawson, 2011b: Representing the ice fall speed in climate models: Results from Tropical Composition, Cloud and Climate Coupling (TC4) and the Indirect and Semi-Direct Aerosol Campaign (ISDAC). *J. Geophys. Res.*, **116**, D00T03, doi:10.1029/2010JD015433.

Morrison, H., and J. A. Milbrandt, 2015: Parameterization of cloud microphysics based on the prediction of bulk ice particle properties. Part I: Scheme description and idealized tests. *J. Atmos. Sci.*, **72**, 287–311, doi:10.1175/JAS-D-14-0065.1.

Brought to you by University of Alabama in Huntsville | Unauthenticated | Downloaded 02/05/25 05:57 PM UTC

——, ——, G. H. Bryan, K. Ikeda, S. A. Tessendorf, and G. Thompson, 2015: Parameterization of cloud microphysics based on the prediction of bulk ice particle properties. Part II: Case study comparisons with observations and other schemes. *J. Atmos. Sci.*, **72**, 312–339, doi:10.1175/JAS-D-14-0066.1.

Moss, S. J., and D. W. Johnson, 1994: Aircraft measurements to validate and improve numerical model parameterization of ice to water ratios in clouds. *Atmos. Res.*, **34**, 1–25, doi:10.1016/0169-8095(94)90078-7.

Nagel, D., U. Maixner, W. Strapp, and M. Wasey, 2007: Advancements in techniques for calibration and characterization of in situ optical particle measuring probes, and applications to the FSSP-100 probe. *J. Atmos. Oceanic Technol.*, **24**, 745–760, doi:10.1175/JTECH2006.1.

Nasiri, S. L., B. A. Baum, A. J. Heymsfield, P. Yang, M. R. Poellot, D. P. Kratz, and Y. Hu, 2002: The development of midlatitude cirrus models for MODIS using FIRE-I, FIRE-II, and ARM in situ data. *J. Appl. Meteor.*, **41**, 197–217, doi:10.1175/1520-0450(2002)041<0197:TDOMCM>2.0.CO;2.

Noone, K. J., J. A. Ogren, J. Heintzenberg, R. J. Charlson, and D. S. Covert, 1988: Design and calibration of a counterflow virtual impactor for sampling of atmospheric fog and cloud droplets. *J. Aerosp. Sci. Technol.*, **8**, 235–244, doi:10.1080/02786828808959186.

Norment, H., 1985: Calculation of water drop trajectories to and about arbitrary three dimensional lifting and non-lifting bodies in potential airflow. NASA Tech. Rep. NASA-CR-3935, 168 pp. [NTIS N87-11694/3/GAR.]

——, 1988: Three-dimensional trajectory analysis of two drop sizing instruments: PMS* OAP and PMS* FSSP. *J. Atmos. Oceanic Technol.*, **5**, 743–756, doi:10.1175/1520-0426(1988)005<0743:TDTAOT>2.0.CO;2.

Nousiainen, T., and G. M. McFarquhar, 2004: Light scattering by quasi-spherical ice crystals. *J. Atmos. Sci.*, **61**, 2229–2248, doi:10.1175/1520-0469(2004)061<2229:LSBQIC>2.0.CO;2.

Paluch, I. R., and D. G. Baumgardner, 1989: Entrainment and fine-scale mixing in continental convective cloud. *J. Atmos. Sci.*, **46**, 261–278, doi:10.1175/1520-0469(1989)046<0261:EAFSMI>2.0.CO;2.

Pinnick, R. G., and H. J. Auvermann, 1979: Response characteristics of Knollenberg light-scattering aerosol counters. *J. Aerosol Sci.*, **10**, 55–74, doi:10.1016/0021-8502(79)90136-8.

Pinsky, M., and A. Khain, 1997: Formation of inhomogeneity in drop concenctration induced by the inertia of drops falling in a turbulent flow, and the influence of the inhomogeneity on the drop spectrum broadening. *Quart. J. Roy. Meteor. Soc.*, **123**, 165–186, doi:10.1002/qj.49712353707.

Platnick, S., J. Y. Li, M. D. King, H. Gerber, and P. V. Hobbs, 2001: A solar reflectance method for retrieving the optical thickness and droplet size of liquid water clouds over snow and ice surfaces. *J. Geophys. Res.*, **106**, 15 185–15 199, doi:10.1029/2000JD900441.

Pruppacher, H. R., and J. D. Klett, 1997: *Microphysics of Clouds and Precipitation*. 2nd ed. Kluwer Academic, 954 pp.

Ramaswamy, V., and V. Ramanathan, 1989: Solar absorption by cirrus clouds and the maintenance of the tropical upper troposphere thermal structure. *J. Atmos. Sci.*, **46**, 2293–2310, doi:10.1175/1520-0469(1989)046<2293:SABCCA>2.0.CO;2.

Reisner, J., R. M. Rasmussen, and R. T. Bruintjes, 1998: Explicit forecasting of supercooled liquid water in winter storms using the MM5 mesoscale model. *Quart. J. Roy. Meteor. Soc.*, **124**, 1071–1107, doi:10.1002/qj.49712454804.

Reuter, A., and S. Bakan, 1998: Improvements of cloud particle izing with a 2D-Grey probe. *J. Atmos. Oceanic Technol.*, **15**, 1196–1203, doi:10.1175/1520-0426(1998)015<1196:IOCPSW>2.0.CO;2.

Rosenberg, P. D., A. R. Dean, P. I. Williams, J. R. Dorsey, A. Minikin, M. A. Pickering, and A. Petzold, 2012: Particle sizing calibration with refractive index correction for light scattering optical particle counters and impacts upon PCASP and CDP data collected during the Fennec campaign. *Atmos. Meas. Tech.*, **5**, 1147–1163, doi:10.5194/amt-5-1147-2012.

Rotstayn, L. D., 1997: A physically based scheme for the treatment of stratiform clouds and precipitation in large-scale models. Part I. Description and evaluation of the microphysical processes. *Quart. J. Roy. Meteor. Soc.*, **123**, 1227–1282.

Schiller, C., M. Krämer, A. Afchine, N. Spelten, and N. Sitnikov, 2008: Ice water content in Arctic, midlatitude and tropical cirrus. *J. Geophys. Res.*, **113**, D24208, doi:10.1029/2008JD010342.

Schmitt, C. G., and A. J. Heymsfield, 2009: The size distribution and mass-weighted terminal velocity of low-latitude tropopause cirrus crystal populations. *J. Atmos. Sci.*, **66**, 2013–2028, doi:10.1175/2009JAS3004.1.

——, and ——, 2010: The dimensional characteristics of ice crystal aggregates from fractal geometry. *J. Atmos. Sci.*, **67**, 1605–1616, doi:10.1175/2009JAS3187.1.

Schumann, U., B. Mayer, K. Gierens, S. Unterstrasser, P. Jessberger, A. Petzold, and J. F. Gayet, 2011: Effective radius of ice particles in cirrus and contrails. *J. Atmos. Sci.*, **68**, 300–321, doi:10.1175/2010JAS3562.1.

Shupe, M. D., T. Uttal, and S. Y. Matrosov, 2005: Arctic cloud microphysics retrievals from surface-based remote sensors at SHEBA. *J. Appl. Meteor.*, **44**, 1544–1562, doi:10.1175/JAM2297.1.

Skamarock, W. C., and Coauthors, 2008: A description of the Advanced Research WRF version 3. NCAR Tech. Note NCAR/TN-475+STR, 113 pp., doi:10.5065/D68S4MVH.

SPEC, 2012: CPIview Quicklook and Extractor: CPI data processing software. SPEC, 33 pp., http://www.specinc.com/sites/default/files/software_and_manuals/CPI_Post%20Processing%20Software%20Manual_rev1.2_20120116.pdf.

Straka, J. M., and E. R. Mansell, 2005: A bulk microphysics parameterization with multiple ice precipitation categories. *J. Appl. Meteor.*, **44**, 445–466, doi:10.1175/JAM2211.1.

Strapp, J. W., F. Albers, A. Reuter, A. V. Korolev, U. Maixner, E. Rashke, and Z. Vukovic, 2001: Laboratory measurements of the response of a PMS OAP-2DC. *J. Atmos. Oceanic Technol.*, **18**, 1150–1170, doi:10.1175/1520-0426(2001)018<1150:LMOTRO>2.0.CO;2.

Stubenrauch, C. J., A. Chedin, G. Radel, N. A. Scott, and S. Serrar, 2006: Cloud properties and their seasonal and diurnal variability from TOVS path-B. *J. Climate*, **19**, 5531–5553, doi:10.1175/JCLI3929.1.

Sulia, K. J., and J. Y. Harrington, 2011: Ice aspect ratio influences on mixed-phase clouds: Impacts on phase partitioning in parcel models. *J. Geophys. Res.*, **116**, D21309, doi:10.1029/2011JD016298.

Szeto, K. K., and R. E. Stewart, 1997: Effects of melting on frontogenesis. *J. Atmos. Sci.*, **54**, 689–702, doi:10.1175/1520-0469(1997)054<0689:EOMOF>2.0.CO;2.

Thompson, G., R. M. Rasmussen, and K. Manning, 2004: Explicit forecasts of winter precipitation using an improved bulk microphysics scheme. Part I: Description and sensitivity analysis. *Mon. Wea. Rev.*, **132**, 519–542, doi:10.1175/1520-0493(2004)132<0519:EFOWPU>2.0.CO;2.

——, P. R. Field, R. M. Rasmussen, and W. D. Hall, 2008: Explicit forecasts of winter precipitation using an improved bulk mi-

Brought to you by University of Alabama in Huntsville | Unauthenticated | Downloaded 02/05/25 05:57 PM UTC

crophysics scheme. Part II: Implementation of a new snow parameterization. *Mon. Wea. Rev.*, **136**, 5095–5115, doi:10.1175/2008MWR2387.1.

Twohy, C. H., and D. Rogers, 1993: Airflow and water drop trajectories at instrument sampling points around the Beechcraft King Air and Lockheed Electra. *J. Atmos. Oceanic Technol.*, **10**, 566–578, doi:10.1175/1520-0426(1993)010<0566:AAWDTA>2.0.CO;2.

——, A. J. Schanot, and W. A. Cooper, 1997: Measurement of condensed water content in liquid and ice clouds using an airborne counterflow virtual impactor. *J. Atmos. Oceanic Technol.*, **14**, 197–202, doi:10.1175/1520-0426(1997)014<0197:MOCWCI>2.0.CO;2.

Twomey, S., Eds., 1977: *Introduction to the Mathematics of Inversion in Remote Sensing and Indirect Measurements*. Vol. 3, *Developments in Geomathematics*, Elsevier, 237 pp.

Um, J., and G. M. McFarquhar, 2007: Single-scattering properties of aggregates of bullet rosettes in cirrus. *J. Appl. Meteor. Climatol.*, **46**, 757–775, doi:10.1175/JAM2501.1.

——, and ——, 2009: Single-scattering properties of aggregates of plates. *Quart. J. Roy. Meteor. Soc.*, **135**, 291–304, doi:10.1002/qj.378.

——, and ——, 2011: Dependence of the single-scattering properties of small ice crystals on idealized shape models. *Atmos. Chem. Phys.*, **11**, 3159–3171, doi:10.5194/acp-11-3159-2011.

——, ——, Y. P. Hong, S.-S. Lee, C. H. Jung, R. P. Lawson, and Q. Mo, 2015: Dimensions and aspect ratios of natural ice crystals. *Atmos. Chem. Phys.*, **15**, 3933–3956, doi:10.5194/acp-15-3933-2015.

van Diedenhoven, B., A. S. Ackerman, B. Cairns, and A. M. Fridlind, 2014: A flexible parameterization for shortwave optical properties of ice crystals. *J. Atmos. Sci.*, **71**, 1763–1782, doi:10.1175/JAS-D-13-0205.1.

Vogelmann, A. M., and T. P. Ackerman, 1995: Relating cirrus cloud properties to observed fluxes: A critical assessment. *J. Atmos. Sci.*, **52**, 4285–4301, doi:10.1175/1520-0469(1995)052<4285:RCCPTO>2.0.CO;2.

Walko, R. L., W. R. Cotton, M. P. Meyers, and J. Y. Harrington, 1995: New RAMS cloud microphysical parameterization. Part I. The single-moment scheme. *Atmos. Res.*, **38**, 29–62, doi:10.1016/0169-8095(94)00087-T.

Weigel, R., and Coauthors, 2016: Thermodynamic correction of particle concentrations measured by underwing probes on fast-flying aircraft. *Atmos. Meas. Tech.*, **9**, 5135–5162, doi:10.5194/amt-9-5135-2016.

Wendisch, M., A. Keil, and A. V. Korolev, 1996: FSSP characterization with monodisperse water droplets. *J. Atmos. Oceanic Technol.*, **13**, 1152–1163, doi:10.1175/1520-0426(1996)013<1152:FCWMWD>2.0.CO;2.

Wood, N., T. L'Ecuyer, F. Bliven, and G. Stephens, 2013: Characterization of video disdrometer uncertainties and impacts on estimates of snowfall rate and radar reflectivity. *Atmos. Meas. Tech.*, **6**, 3635–3648, doi:10.5194/amt-6-3635-2013.

Wu, W., and G. M. McFarquhar, 2016: On the impacts of different definitions of maximum dimension for nonspherical particles recorded by 2DD imaging probes. *J. Atmos. Oceanic Technol.*, **33**, 1057–1072, doi:10.1175/JTECH-D-15-0177.1.

——, ——, L. Xue, H. Morrison, and W. W. Grabowski, 2016: The effectiveness of spectral bin schemes in simulating ice cloud particle size distributions and their variability. *17th Int. Conf. Clouds and Precipitation*, Manchester, United Kingdom, International Commission on Clouds and Precipitation, S1.11, 320, http://www.meeting.co.uk/confercare/iccp2016/Oral%20and%20Poster%20Abstracts.pdf.

Wylie, D., D. L. Jackson, W. P. Menzel, and J. J. Bates, 2005: Trends in global cloud cover in two decades of HIRS observations. *J. Climate*, **18**, 3021–3031, doi:10.1175/JCLI3461.1.

Zhang, J., B. Lei, J. Liu, R. L. Panetta, P. Yang, and G. W. Kattawar, 2016: Optical scattering simulation of ice particles with surface roughness modeled using the Edwards-Wilkinson equation. *J. Quant. Spectrosc. Radiat. Transfer*, **178**, 325–335, doi:10.1016/j.jqsrt.2016.02.013.

Zhao, Y., G. G. Mace, and J. M. Comstock, 2011: The occurrence of particle size distribution bimodality in midlatitude cirrus as inferred from ground-based remote sensing data. *J. Atmos. Sci.*, **68**, 1162–1177, doi:10.1175/2010JAS3354.1.

Zukauskas, A., and J. Ziugzda, 1985: *Heat Transfer of a Cylinder in Crossflow*. G. F. Hewitt, Ed., Hemisphere Publishing, 208 pp.

Brought to you by University of Alabama in Huntsville | Unauthenticated | Downloaded 02/05/25 05:57 PM UTC